

Multibaseline Interferometry Based on Independent Component Analysis and InSAR Combinatorial Modeling for High-Precision DEM Reconstruction

Tengfei Zhang^{ID}, Graduate Student Member, IEEE, Yumin Chen^{ID}, Lu Zhang^{ID}, John P. Wilson^{ID}, Rui Zhu^{ID}, Ruoxuan Chen, and Zhanghui Li

Abstract—Digital elevation models (DEMs) are essential for national economic development, disaster management, and military applications. Multi baseline interferometric synthetic aperture radar (MB-InSAR) technology has proven to be an effective method for DEM reconstruction. However, the presence of atmospheric noise and other residual signals introduces unavoidable errors in the phase observations, and most MB-InSAR DEMs are generated using a single empirical mathematical model that ignores the influence of deformation factors. To compensate for these limitations, we propose spatial independent component analysis (sICA) phase separation and interferometric synthetic aperture radar (InSAR) combinatorial modeling (CM) InSAR CM (ISCM). The sICA was used for phase separation, resulting in clear InSAR signals and reducing atmospheric noise and other residual signal interference; then, the effects of linear deformation, seasonal deformation, and environmental factors were considered in the InSAR modeling. In the experiments, a total of 19 TerraSAR-X images from San Diego, USA (SD), and 18 PAZ images from Yan'an, China (YA), were selected to generate DEMs with resolutions of 3 and 6 m, respectively. The accuracy of the DEM generated by ISCM was evaluated using the photogrammetric DEM, and the root-mean-square errors (RMSEs) of the elevation are 3.20 m for SD and 4.41 m for YA, with an improvement of 30.8%–44.9% and 21.9%–38.4%, respectively, compared to the traditional MB-InSAR method. In addition, ICESat/GLAS data collected in YA were used for further validation with an improvement of 13.7%–29.5%. The DEM generated by ISCM has significant advantages in improving accuracy and preserving terrain features, providing theoretical support for global high-precision DEM mapping.

Received 9 December 2024; revised 24 January 2025; accepted 12 February 2025. Date of publication 14 February 2025; date of current version 28 February 2025. This work was supported in part by the National Natural Science Foundation of China under Grant 42471456; in part by the National Key Research and Development Program of China under Grant 2022YFB3902300; and in part by the Fundamental Research Funds for the Central Universities, China, under Grant 2042022dx0001. (Corresponding author: Yumin Chen.)

Tengfei Zhang, Yumin Chen, Ruoxuan Chen, and Zhanghui Li are with the School of Resource and Environmental Sciences, Wuhan University, Wuhan 430079, China (e-mail: tengfeizhang@whu.edu.cn; ymchen@whu.edu.cn; 2023202050017@whu.edu.cn; lizhanghui@whu.edu.cn).

Lu Zhang is with the State Key Laboratory of Information Engineering in Surveying, Mapping and Remote Sensing, Wuhan University, Wuhan 430079, China (e-mail: luzhang@whu.edu.cn).

John P. Wilson is with the Spatial Sciences Institute, University of Southern California, Los Angeles, CA 90089 USA (e-mail: jpwilson@usc.edu).

Rui Zhu is with the Institute of High Performance Computing (IHPC), Agency for Science, Technology and Research (A*STAR), Singapore 138632 (e-mail: zhur@ihpc.a-star.edu.sg).

Digital Object Identifier 10.1109/TGRS.2025.3542614

Index Terms—Digital elevation models (DEMs), independent component analysis (ICAs), interferometric synthetic aperture radar (InSAR) modeling, multi baseline, phase separation.

I. INTRODUCTION

HIGH-PRECISION digital elevation models (DEMs) are crucial for national economic development, disaster prevention and control, urban operation and management, and military applications [1], [2], [3]. It plays an essential role in geoinformation and remote sensing [4]. However, the freely available global shuttle radar DEM (SRTM) with a 30-m resolution was collected in 2000 [5], [6] and cannot accurately reflect current topographic conditions. Therefore, the generation of high-precision DEM is important for research. The most effective methods for DEM generation include topographic mapping, ground surveying, and light detection and ranging (LiDAR) [7]. While these techniques meet the accuracy requirements for DEM generation, their limited point density, spatial coverage, and temporal resolution have limited their use in large-scale DEM generation. Interferometric synthetic aperture radar (InSAR) technology is an effective method for acquiring high-precision DEM due to its all-day and all-weather capability, cloud penetration, and high spatial-temporal resolution [8].

DEM generation using InSAR technology mainly includes two-pass, multibaseline InSAR (MB-InSAR), and bistatic InSAR methods. However, the traditional two-pass method is affected by spatial-temporal decorrelation, atmospheric noise, and deformation effects, which can significantly degrade the quality of the DEM [9]. With the continuous development of high-resolution (HR) satellites on different platforms and orbits, such as COSMO-SkyMed with better than 3-m resolution from Italian Space Agency (ASI), and TerraSAR-X and TanDEM-X with better than 3-m resolution from German Aerospace Center (DLR), researchers have devoted their efforts to the study of MB-InSAR. Berardino et al. [10] introduced the small baseline subset (SBAS), which can separate the deformation and residual topography from the InSAR phase. Samsonov et al. [11] proposed an optimized SBAS approach by adjusting the DEM errors and deformation rates, which is appropriate for ALOS-PALSAR data. Zhao et al. [12] improved the accuracy of the DEM

generated from TerraSAR-X data by introducing a reference DEM. Subsequently, a new approach based on a polynomial model (PM) was introduced to estimate the DEM errors after time series inversion [13]. Building on this, Zhang et al. [14] proposed a PM model combination with ascending and descending data to generate DEM over Heifangtai, China. In terms of bistatic interferometry, Lachaise et al. [15] proposed a dual-baseline phase unwrapping correction (DB-PUC) framework, and the experimental results show that the DB-PUC framework processes TanDEM-X data with high precision. Dong et al. [16] introduced the cascaded multibaseline approach to address the issues of perpendicular baseline sensitivity and phase unwrapping. The bistatic InSAR effectively improves the accuracy of the DEM [17], but it still suffers from the difficulty of phase unwrapping in complex terrain areas and the difficulty of removing the erroneous fringes caused by baseline errors. The MB-InSAR technique, as a common method for high-precision DEM generation, involves the following basic research idea. By combining the advantages of easy phase unwrapping with short baselines and high accuracy of topographic measurement from corresponding long baseline interferograms, the complexity of phase unwrapping is effectively reduced, leading to improved inversion accuracy for topographic measurement.

However, DEM generation using MB-InSAR technology is still limited by the presence of atmospheric noise, other residual signals, and deformation modeling errors. Atmospheric noise reduction in the InSAR signal processing needs to be further addressed, as most methods for handling the atmosphere and noise require the use of external atmospheric data and sophisticated atmospheric modeling [18], [19], [20]. The phase signals acquired by InSAR technology mainly contain both deformation and elevation information, and most MB-InSAR DEM generation methods rely on a single purely mathematical empirical model (i.e., a linear model (LM) and seasonal model (SM) or PM) and ignore the influence of deformation factors, which can introduce errors into the DEM if the deformation phase cannot be accurately separated from the interferogram [21]. In fact, due to the large weight of the deformation coefficients and the small weight of the topography coefficients in the phase equations, deformation errors in the millimeter range can lead to elevation errors of several meters or even tens of meters [3].

The independent component analysis (ICA) algorithm, first explored in the field of neural networks, has the ability to separate the signal without any prior information. It has been applied to signal separation and feature extraction [22]. Researchers have attempted to apply ICA technology to InSAR phase separation and surface deformation extraction [23], [24]. Peng et al. [25] introduced a spatial-temporal InSAR prediction model using ICA and long short-term memory (LSTM). In addition, nonparametric estimation of DEM errors using the ICA technique is essential to remove residual terrain phases from interferograms [26]. However, the advantages of ICA for high-precision DEM generation are unclear, and it is important to know how to combine the benefits of signal identification and InSAR modeling.

Based on this analysis, the main challenges in implementing the combination of ICA and MB-InSAR techniques to produce high-precision DEMs are as follows: 1) MB-InSAR techniques are severely limited by the atmospheric noise, other residual signals, and deformation modeling errors, how to further understand the characteristics of the signals is the main factors to improve the phase quality; 2) most of the current studies ignore the influence of the deformation phase on the terrain and how to combine the separated phase and the deformation phase is the key to accurate elevation measurement; and 3) it is necessary to further optimize ICA separation techniques and InSAR modeling methods.

In this study, to compensate for these limitations, we proposed spatial ICA (sICA) phase separation and InSAR combinatorial modeling (ISCM) to address errors in the MB-InSAR DEM reconstruction. The sICA was used to separate the signals according to the spatial and temporal distribution characteristics of the InSAR phase. Considering the inaccuracy of ICA separation when deformation and topography phase are spatially correlated, we remove the atmospheric noise and other residual signals directly from the phase observations; then, during the InSAR modeling process, we considered the effects of linear deformation, seasonal deformation, and environmental factors, and an ISCM was proposed, which improves the accuracy of the deformation modeling and the precision of obtaining the DEM.

II. METHODOLOGY

This article proposes the ISCM method to solve the problems associated with atmospheric noise, other residual signals, and inaccurate deformation modeling in MB-InSAR DEM generation. Specifically, the ISCM method includes the following steps: 1) InSAR differential interferometric phase generation; 2) ICA phase separation (IS); 3) InSAR combinatorial modeling (CM); and 4) high-precision DEM generation and precision evaluation. The end-to-end workflow is summarized, as shown in Fig. 1.

A. InSAR Differential Interferometric Phase Generation

During the process of DEM generation by MB-InSAR, the presence of dense interferometric fringes resulting from the topography phase can significantly affect the accuracy of the phase unwrapping. To address this issue, several researchers have proposed a two-step data processing where the topography phase can be removed by using a low-resolution (LR) reference DEM [expressed as $h_{\text{ref}}(x, y)$], and then, the phase equation is used to solve the HR residual elevation information $\Delta h(x, y)$. High-precision surface elevation can be described as follows [18]:

$$z(x, y) = h_{\text{ref}}(x, y) + \Delta h(x, y). \quad (1)$$

Suppose that $N+1$ SAR images are acquired over the same area, resulting in M interferometric pairs. The interferometric phase $\delta\varphi_i^m$ at the i th pixel (x, y) in the m th interferogram can

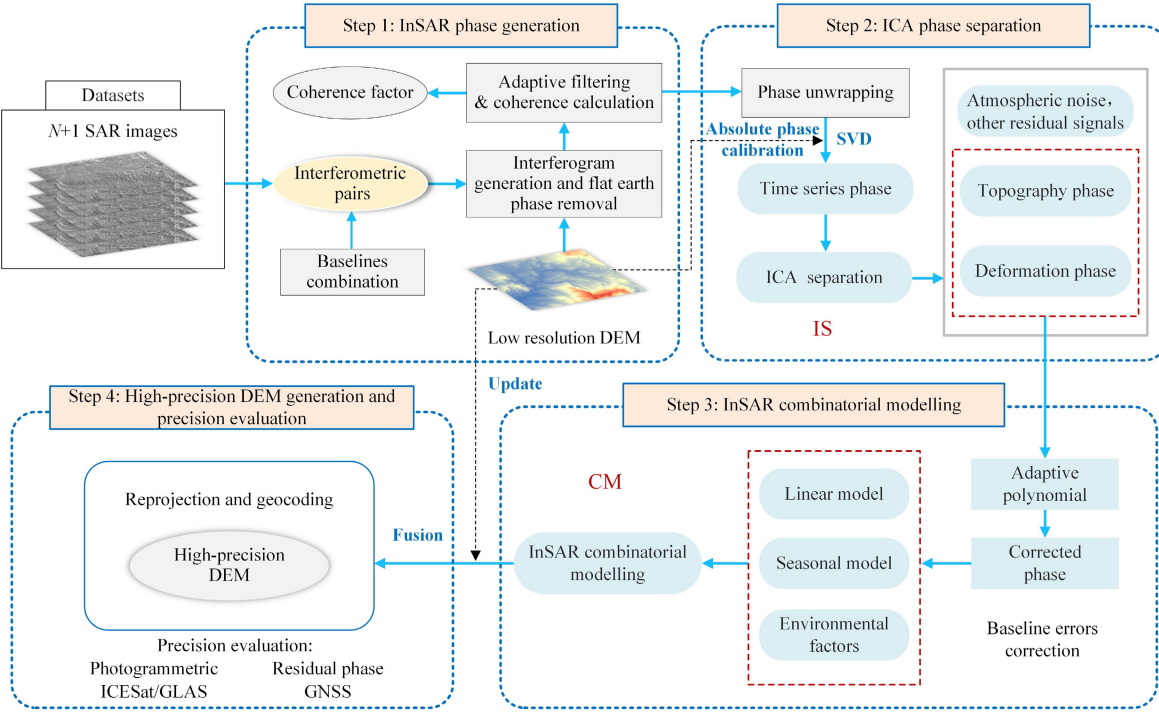


Fig. 1. End-to-end workflow of the ISCM. Step 1: InSAR phase generation. Step 2: ICA phase separation. Step 3: ISCM. Step 4: high-precision DEM generation and precision evaluation.

be described as follows [10], [27], [28], [29]:

$$\delta\varphi_i^m = \delta\varphi_{\text{def}}^i + \delta\varphi_{\text{topo}}^i + \delta\varphi_{\text{orbit}}^i + \delta\varphi_{\text{atm}}^i + \delta\varphi_{\text{noise}}^i + \delta\varphi_{\text{hp}}^i \\ \approx \frac{4\pi}{\lambda} \Delta d(x, y) + \frac{4\pi B_{\perp}^m}{\lambda R \sin \theta} \Delta h(x, y) + \delta\varphi_{\text{res}}^m(x, y) \quad (2)$$

where $\delta\varphi_{\text{def}}^i$ is the deformation phase; λ and $\Delta d(x, y)$ correspond to the radar wavelength and deformation along the line-of-sight (LOS) direction, respectively; $\delta\varphi_{\text{topo}}^i$ is the topography phase and the contribution related to the residual elevation, the relationship being directly proportional to the perpendicular baseline and inversely proportional to the sine of the angle of incidence; $\delta\varphi_{\text{orbit}}^i$ is the orbit error, the effects of which are generally global and systematic in an interferogram, and the orbital data are used in the interferometric processing by the refinement and flattening; and $\delta\varphi_{\text{res}}^m(x, y)$ is the residual phase, including atmospheric delay phase $\delta\varphi_{\text{atm}}^i$, noise phase $\delta\varphi_{\text{noise}}^i$, and high-pass (HP) deformation phase $\delta\varphi_{\text{hp}}^i$. The residual phase consists mainly of signals that are not fully fit by the data preprocessing and InSAR modeling [30]. The function between topography phase and height can be expressed as [12]

$$\delta\varphi_{\text{topo}}^i = \frac{4\pi B_{\perp}^m}{\lambda R \sin \theta} \Delta h(x, y) \quad (3)$$

where B_{\perp}^m is the perpendicular baseline, the baseline represents the spatial distance and direction between two SAR observations, and the baseline is critical for detecting changes in topography and resolving the direction of surface deformation; R is the sensor-target distance; θ is the radar incidence angle; and $\Delta h(x, y)$ is the residual elevation, which represents the difference between HR DEM and LR DEM.

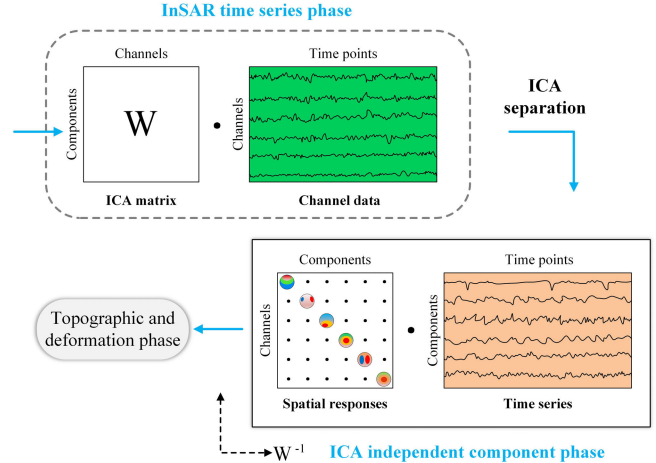


Fig. 2. ICA time series phase separation.

B. ICA InSAR Phase Separation

The InSAR time series phase of the study area was used as input and sICA was used to separate the signals (as shown in Fig. 2). Since ICA can better explore the spatial-temporal distribution characteristics of signals through time series, the selected m interferograms are first transformed into time series according to singular value decomposition (SVD) [31]. The $N + 1$ InSAR time series phase can be represented as

$$X = AS \quad (4)$$

where X is the time series mixed signal, which can be regarded as the time series phase of InSAR; A is the mixing

matrix, which is the time series of all the independent components; and S is the source signal, which represents the combination of the spatial response of all the independent components. The spatial response represents the variation and distribution characteristics of the radar signal in the spatial dimension, reflecting changes in the InSAR phase of the signal at different geographical locations that may be caused by surface deformation, topographic changes, atmospheric noise, and other residual signals. Suppose that a total of C high coherence points were selected in the YA, the mixed signal X can be represented as $X_{(N+1) \times C} = [\varphi_C^1 \varphi_C^2 \cdots \varphi_C^{N+1}]^T$, where φ_C^1 , φ_C^2 , and φ_C^{N+1} indicate the phase at different moments. The mixing matrix A can be represented as $A_{(N+1) \times n} = [TS_{N+1}^1 \ TS_{N+1}^2 \ \cdots \ TS_{N+1}^n]$, where TS_{N+1}^1 , TS_{N+1}^2 , and TS_{N+1}^n denote the time series of each independent component and n represents the number of independent components. The source signal S (including the deformation phase φ_{def} , topography phase φ_{topo} , and atmosphere delay phase φ_{atm}) can be expressed as

$$\begin{aligned} S_{n \times C} &= [\text{SR}_C^1 \ \text{SR}_C^2 \ \cdots \ \text{SR}_C^n]^T \\ &= \begin{bmatrix} \varphi_{\text{def}}^1 & \varphi_{\text{topo}}^1 & \varphi_{\text{atm}}^1 & \cdots & \varphi_{\text{hp}}^1 \\ \varphi_{\text{def}}^2 & \varphi_{\text{topo}}^2 & \varphi_{\text{atm}}^2 & \cdots & \varphi_{\text{hp}}^2 \\ \vdots & \vdots & \vdots & \ddots & \vdots \\ \varphi_{\text{def}}^C & \varphi_{\text{topo}}^C & \varphi_{\text{atm}}^C & \cdots & \varphi_{\text{hp}}^C \end{bmatrix}^T \end{aligned} \quad (5)$$

where SR_C^1 , SR_C^2 , and SR_C^n denote the spatial response of each independent component, and at this point, the InSAR phase can be described as follows:

$$\begin{aligned} X_{(N+1) \times C} &= A_{(N+1) \times n} S_{n \times C} = A_{(N+1) \times n} \\ &\times \begin{bmatrix} \varphi_{\text{def}}^1 & \varphi_{\text{topo}}^1 & \varphi_{\text{atm}}^1 & \cdots & \varphi_{\text{hp}}^1 \\ \varphi_{\text{def}}^2 & \varphi_{\text{topo}}^2 & \varphi_{\text{atm}}^2 & \cdots & \varphi_{\text{hp}}^2 \\ \vdots & \vdots & \vdots & \ddots & \vdots \\ \varphi_{\text{def}}^C & \varphi_{\text{topo}}^C & \varphi_{\text{atm}}^C & \cdots & \varphi_{\text{hp}}^C \end{bmatrix}^T. \end{aligned} \quad (6)$$

The different signal types represented in the InSAR phase are independent of each other, so the FastICA can be used to separate the independent components from the time series. The independent components can be expressed as $\text{IC}^n = \text{SR}^n \times \text{TS}^n$. In principle, the residual elevation could be obtained directly by using the signals associated with the topographic phase after phase separation [26], but considering that the deformation phase and the topography phase may interfere with each other if they are correlated, the atmospheric noise and other residual signals were removed. The time series phases are then transformed into m interferograms based on the relationship between the phases. Consequently, the phase after ICA separation and removal of atmospheric noise and other residual signals $\delta\varphi_i^m$ can be expressed as

$$\begin{aligned} \delta\varphi_i^m &= \text{SR}_{\text{def}}^i \times \text{TS}_{\text{def}}^m + \text{SR}_{\text{topo}}^i \times \text{TS}_{\text{topo}}^m \\ &\approx \frac{4\pi}{\lambda} \Delta d(x, y) + \frac{4\pi B_\perp^m}{\lambda R \sin \theta} \Delta h(x, y) + \delta\varphi_{\text{res}}^m(x, y). \end{aligned} \quad (7)$$

C. InSAR Combinatorial Modeling

The baseline is a critical parameter in the InSAR DEM generation. Baseline errors were corrected using the adaptive

polynomial fitting after ICA separation [32], [33], [34]. The phase after the baseline error correction (BC) can be described as $\delta\varphi_i^m|_{\text{BC}}$. After obtaining accurate InSAR phase observations, it is crucial to establish a functional model that relates the differential interferometric phase to topography and deformation. Du et al. [21] used simulated experiments to test the accuracy of commonly used InSAR models and showed that the choice of deformation model has a critical effect on the residual elevation generation. The surface deformation associated with seasonal changes can be described as a combination of linear and seasonal components [35], [36]. Besides, the formation of surface deformation is closely related to groundwater level fluctuations, which are mainly influenced by environmental factors [37], [38]. Therefore, in the process of InSAR DEM generation, we consider the linear deformation, seasonal deformation, and environmental factors to generate the residual elevation, which can be expressed as

$$\varphi_{\text{def}}^i = \frac{4\pi}{\lambda} (\Delta d_{\text{Li}}^i + \Delta d_{\text{Se}}^i + \Delta d_{\text{EF}}^i) \quad (8)$$

where Δd_{Li}^i denotes the linear deformation, Δd_{Se}^i is the seasonal deformation, and Δd_{EF}^i denotes the environmental factor deformation. The interferometric phase using the InSAR combinatorial model can be expressed as

$$\begin{aligned} &\delta\varphi_i^m|_{\text{BC}} \\ &\approx \frac{4\pi}{\lambda} \left(\sum_{t_{A+1}}^{t_B} v_k(t_k - t_{k-1}) + \alpha_1 \left[\sin\left(\frac{2\pi}{T} t_B\right) - \sin\left(\frac{2\pi}{T} t_A\right) \right] \right. \\ &\quad + \alpha_2 \left[\cos\left(\frac{2\pi}{T} t_B\right) - \cos\left(\frac{2\pi}{T} t_A\right) \right] \\ &\quad \left. + e_1[\text{Tem}(t_B) - \text{Tem}(t_A)] + e_2[\text{Pre}(t_B) - \text{Pre}(t_A)] \right) \\ &\quad + \frac{4\pi B_\perp^m}{\lambda R \sin \theta} \Delta h(x, y) + \delta\varphi_{\text{res}}^m(x, y) \end{aligned} \quad (9)$$

where t_B and t_A are the acquisition times of the differential interferogram; v_k represents the linear deformation rate between images; t_k and t_{k-1} are the time corresponding to the linear deformation rate at different moments and its previous moment, respectively; α_1 and α_2 denote the coefficients of seasonal deformation, respectively; T is the length of the year, which can be considered as 365.25 days; e_1 and e_2 denote the coefficients of environmental deformation; and Tem and Pre denote the average monthly temperature and precipitation, respectively. In principle, at least $N + 5$ interferometric pairs, the equations can be solved, and to avoid the model overparameterization causing problems in the solution, we suggest preferentially using the conditional condition number $\text{Cond}_\infty(B) = \|B\|_\infty \|B^{-1}\|_\infty$ to determine the ill-conditioned of the matrix, and B is the coefficient matrix of the set of phase equations. Then, least squares (LSSs) and SVD [14] can be used to estimate the unknown parameter $X = [v_1 \ v_2 \ \cdots \ v_N \ \alpha_1 \ \alpha_2 \ e_1 \ e_2 \ \Delta h(x, y)]$.

D. High-Precision DEM Generation and Precision Evaluation

When the model parameters are obtained, the high-precision DEM can be generated using (1). However, the time series InSAR technology based on high coherence points has limitations due to spatial-temporal incoherence or geometric distortions. To address this, this study uses an interpolated fusion approach to improve the accuracy [39]. The acquired DEM is then reprojected and geocoded to the WGS-84 coordinate system to facilitate the understanding and interpretation of the acquired geographic information.

The DEMs generated by the ISCM method were compared with several traditional methods. The LM method, known for its dense time sampling interval, is a classical residual elevation generation algorithm. The SM method, on the other hand, is more suitable for areas with complex topography and has been used for regional permafrost deformation inversion and DEM generation. The PM method is known for its suitability for nonlinear data and high accuracy in DEM generation. The persistent scatterer interferometry (PSI) method is known for its high accuracy in deformation estimation and handling of SAR signal decorrelation [40], [41]. The maximum elevation error (E_{\max}), root-mean-square error (RMSE), mean absolute error (MAE), and 90% linear point-to-point error (LE90) were used to validate the elevation accuracy of ISCM. The standard deviation (STD) of the residual phase was used to evaluate the InSAR modeling. In addition, the MAE of the terrain features was used to evaluate the preservation of the terrain features

$$E_{\max} = \max(\text{abs}(y_i - \hat{y}_i)) \quad (10)$$

$$\text{RMSE} = \sqrt{\frac{1}{j} \sum_{i=1}^j (y_i - \hat{y}_i)^2} \quad (11)$$

$$\text{MAE} = \frac{1}{j} \sum_{i=1}^j |(y_i - \hat{y}_i)| \quad (12)$$

$$\text{STD} = \sqrt{\frac{1}{j} \sum_{i=1}^j (y_i - \bar{y}_i)^2} \quad (13)$$

$$E_{tf} = \frac{1}{j} \sum_{i=1}^j |(t_i - \hat{t}_i)| \quad (14)$$

where j represents the number of pixels, y_i represents the true value, \hat{y}_i represents the model generation value, \bar{y}_i represents the mean of the observed data, t_i is the terrain parameter generated from the original elevation, and \hat{t}_i is the terrain parameter generated from different models.

III. EXPERIMENTS AND RESULTS

A. YA and Data Preprocessing

Two typical study areas, San Diego, USA (SD), and Yan'an City, Loess Plateau, China (YA), were selected as test areas (as shown in Figs. 3 and 4). The purple rectangles in Figs. 3(a) and 4(a) denote the spatial coverage of the (descending) TerraSAR-X and PAZ data, and the yellow rectangles are two test areas of interest. Both the test areas

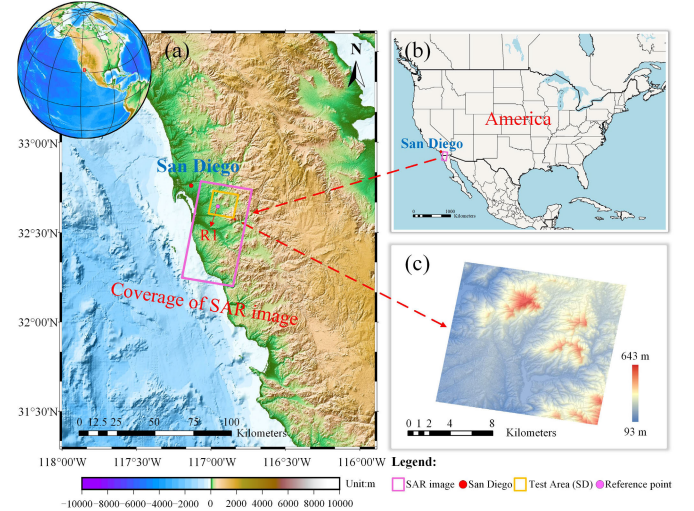


Fig. 3. Map of the study area (SD). (a) Coverage of SAR image. (b) Location of SD on the map of the USA. (c) ALOS 12.5-m DEM of the YA.

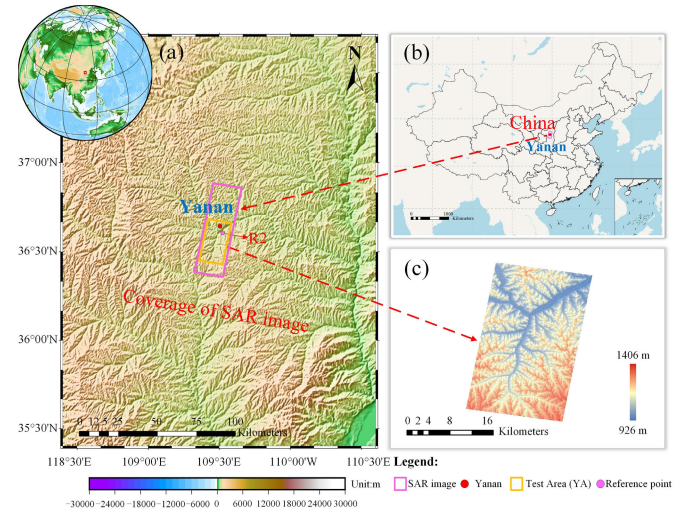


Fig. 4. Map of the study area (YA). (a) Coverage of SAR image. (b) Location of YA on the map of China. (c) ALOS 12.5-m DEM of the YA.

are rich in topography and geomorphology, characterized by high surface relief due to the presence of mountains, plains, hills, and a dense network of rivers and lakes, making them ideal for high-precision DEM studies and mapping. A total of 19 TerraSAR-X images were collected in the SD area (from August 8, 2009 to April 29, 2010) and 18 PAZ images were collected in the YA area (from April 8, 2022 to October 21, 2023).

Data preprocessing was performed using GAMMA software, and the spatial-temporal baseline thresholds were set to 400 m and 150 days. To account for the effects of decorrelation noise and to preserve as much of the original image resolution as possible, a 1:1 multilooking was used in the SD area and a 2:1 multilooking was used in the YA area, resulting in a resolution of about 2.05×1.76 m for the SD area and 5.08×4.24 m for the YA area in the WGS-84 north and east directions, respectively [42], [43]. The Goldstein filter was used for further noise reduction.

TABLE I
DATA PARAMETERS USED IN THIS WORK

Data parameters	SD area	YA area
Acquisition time	20090808-20100429	20220408-20231021
Data types (resolution)	TerraSAR-X (3m)	PAZ (6m)
Number	19-view	18-view
Instrument mode	Stripmap	Stripmap Dual
Central incidence angle	39.26°	43.92°
Heading	192.17°	191.91°
Polarization	HH	HH
Orbit direction	Descending	Descending
Scene size	30×50km ²	15×50km ²
Reference DEM	ALOS 12.5m	ALOS 12.5m
Validation DEM	Photogrammetric 3m	Photogrammetric 5m
ICESat/GLAS point	-	128

The topography phase was filtered using ALOS 12.5-m DEM (<https://search.asf.alaska.edu>) [44], [45]. Polynomial fitting models were used to remove orbital errors and minimum cost flow (MCF) was used for phase unwrapping [46]. The reference points for SD and YA are shown as R1 in Fig. 3(c) and R2 in Fig. 4(c), respectively. After removing the less effective interference pairs, the spatial-temporal baseline connection is shown in Fig. 5, and the data parameters used in this work are shown in Table I. Finally, 36 interferometric pairs for the SD and 34 interferometric pairs for the YA are selected for the ISCM experiment. The selected interferometric pairs have smooth phases, continuous and no obvious jumps, stable coherence, and low noise images. Besides, the three-threshold method (coherence threshold, amplitude deviation index, and intensity) was used to extract high coherence points [14], [47].

B. Residual Elevation Estimation by ISCM

1) *ICA Phase Separation*: As described in Section II-B, the FastICA phase separation algorithm was used in the experiments to analyze the changes in the independent components. In the experimental process, the effect of separation number n on the contribution rate was investigated to determine the most effective number of ICA separations. It was found that when the number of separations was 6 for the SD area and 5 for the YA area, the contribution rate (the proportion of the independent components isolated by ICA to the total components) reached 90.2% and 96.5%, respectively [24]. Also, the nonindependent component can be considered as other residual signals. Furthermore, if the number of separations is lower than the optimal number, it becomes difficult to separate the atmosphere and its contribution. Conversely, if the number of separations is higher than the optimal value, it may disrupt the spatial distribution and time series of topography and deformation. Therefore, we considered the optimal number of separations to be 6 for the SD area and 5 for the YA area.

Figs. 6 and 7 show the normalized spatial response and time series of each independent component, respectively. To obtain a physical interpretation of these independent components,

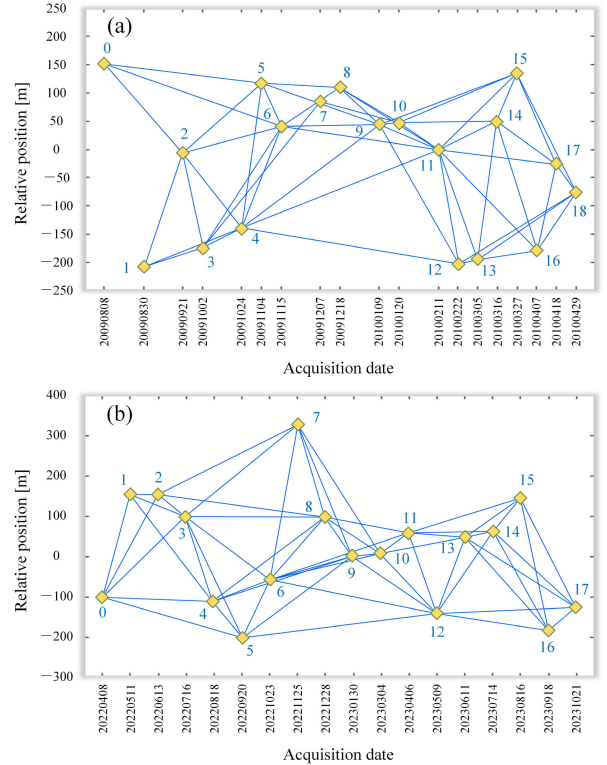


Fig. 5. Spatial-temporal baseline connection. (a) SD area. (b) YA area.

we resolve the deformation and topography using the SBAS method before ICA separation. For the SD area, IC2 showed a spatial alignment with the SBAS residual elevation, indicating that it can be interpreted as the topography phase; IC1, IC3, and IC4 showed a cumulative situation in the time series, as shown by the red arrows in Fig. 6. IC3 showed a simple composition and showed a linear trend, indicating that it can be considered as a linear deformation phase; IC1 and IC4 showed consistent time series and were spatially dominant in the SBAS deformation, indicating that they can be attributed to seasonal and environmental factor-induced deformation phases; in addition, IC5 and IC6 showed clear atmospheric and noise features, with repeated jumps in the range of $[-8, 8]$ radians over time, as shown by the blue dotted lines in Fig. 6, indicating their association with the atmosphere and noise phases. Similarly, for the YA area, IC3 and IC1 can be considered as the topography and linear deformation phases, respectively; IC2 and IC4 can be considered as the seasonal and environmental factor-induced deformation phases; and IC5 can be considered as the atmosphere and noise phases.

In addition, to confirm the accuracy of the physical interpretation, a spatial estimation of the atmosphere and noise is performed using simultaneous GACOS (<http://ceg-research.ncl.ac.U.K./v2/gacos/>) [48], [49]. Therefore, atmosphere and noise can be directly removed after ICA phase separation. For the SD area, the correlations between the deformation and topography phases are small, but for the YA area, the deformation and topography phases have a greater correlation as shown by the red circle as shown in Fig. 7. At this point, deformation and topography are entangled

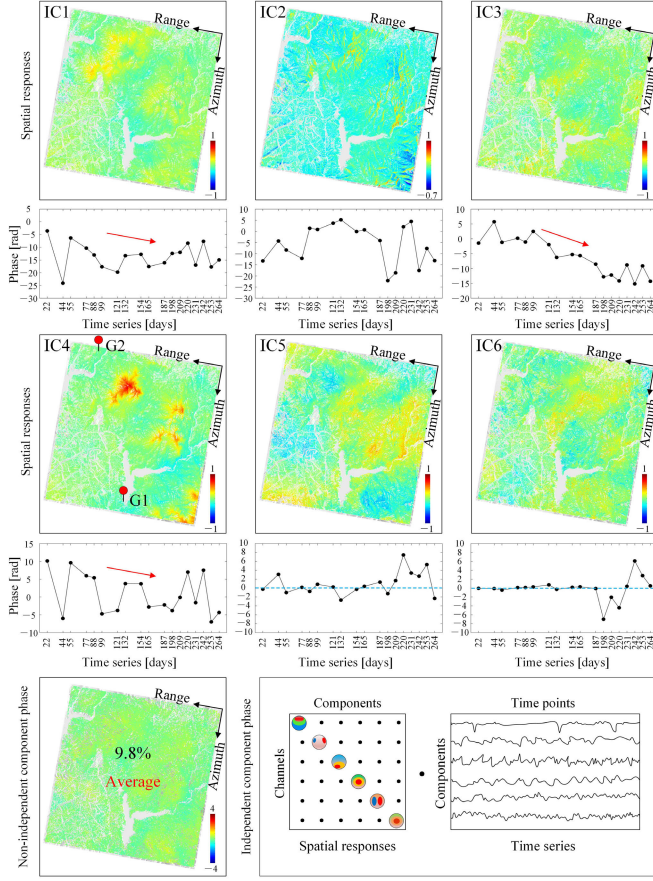


Fig. 6. Spatial response and time series of each independent component for the SD (the top is the spatial response and the bottom is the time series).

with each other, and therefore, the subsequent modeling is important.

2) InSAR Combinatorial Modeling: As mentioned in Section II-C, the baseline errors were corrected using the adaptive polynomial fitting after ICA separation. The average baseline error for both areas is less than 0.5 rad, which is consistent with the magnitude of the baseline error. The environmental factor can be obtained from climate data (<https://www.worldclim.org/data/monthlywth.html>). Fig. 8(a) shows that the residual elevation calculated by ISCM was between $[-28, 38]$ m for SD. The maximum elevation change is 37.5 m, and the largest residual elevation change was observed in steep mountainous areas. For the YA area, the residual elevation is between $[-70, 80]$ m, with a maximum elevation of 69.6 m, and the largest residual elevation change occurred mainly in the urban area of Yanan city [Fig. 8(b)]. This can be attributed to the fact that the PAZ data for the YA area are the latest, covering the period from 2022 to 2023, which has a longer time interval compared to the reference ALOS DEM data collected in 2008. In addition, urban construction has a greater impact on topographic changes, which will be discussed in Section IV-D.

C. High-Precision DEM Generation by ISCM

After obtaining the residual elevations as shown in Fig. 8, the surface elevation can be realized by (1), and the generated

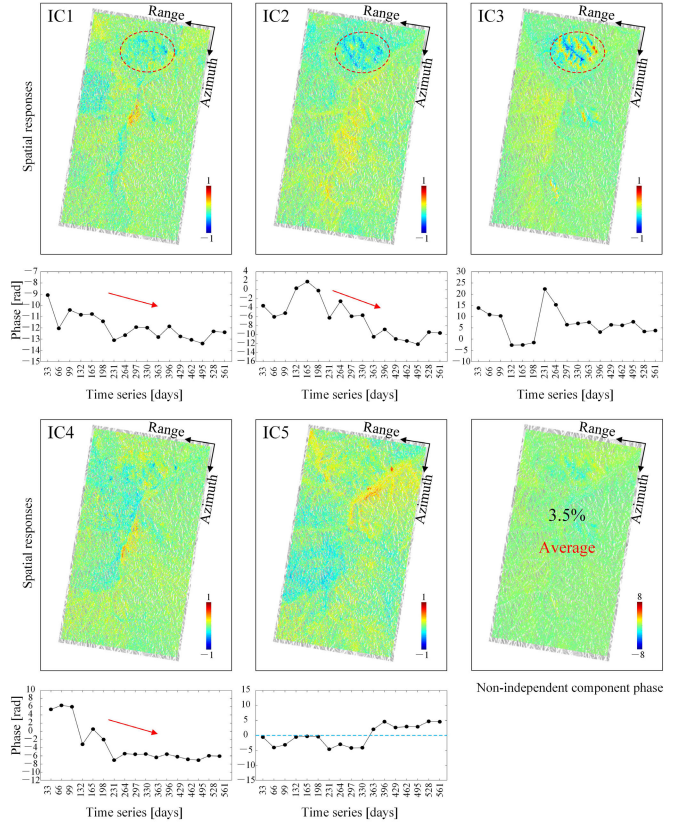


Fig. 7. Spatial response and time series of each independent component for the YA (the top is the spatial response and the bottom is the time series).

DEMs are shown in Figs. 9 and 10. For comparison with the acquired photogrammetric DEMs, the DEMs were resampled to the 3-m resolution for the SD area and 6-m resolution for the YA area. The DEMs generated by ISCM not only effectively reduce the noise present in the SAR-generated DEMs but also improve the visibility of mountains, rivers, and urban areas compared to the traditional LM and PM methods. However, due to the large size of the DEMs generated, the elevation changes in Figs. 9 and 10 may not be apparent from the images alone, although there are obvious differences. In Section III-D, the area E(a) in Fig. 9 and the area E(b) in Fig. 10 are clearly shown to better explore the detail variation.

D. Accuracy Evaluations

1) Accuracy Evaluation Using Photogrammetric DEM:

To verify the elevation accuracy of the DEMs generated by the ISCM method, photogrammetric DEMs with a resolution of 3 m in the SD area (<https://datagateway.nrcs.usda.gov/>) and 6 m in the YA area were collected for validation. The photogrammetric DEMs are located at E(a) in Fig. 9 and E(b) in Fig. 10. All the generated DEMs were geocoded and projected to the WGS-84 coordinate system [50]. From Figs. 11 and 12, the DEMs generated by the traditional LM, SM, PM, and PSI methods contain obvious atmospheric noise and other effects, whereas the DEMs generated by the ISCM method show a high degree of agreement with the photogrammetric DEM.

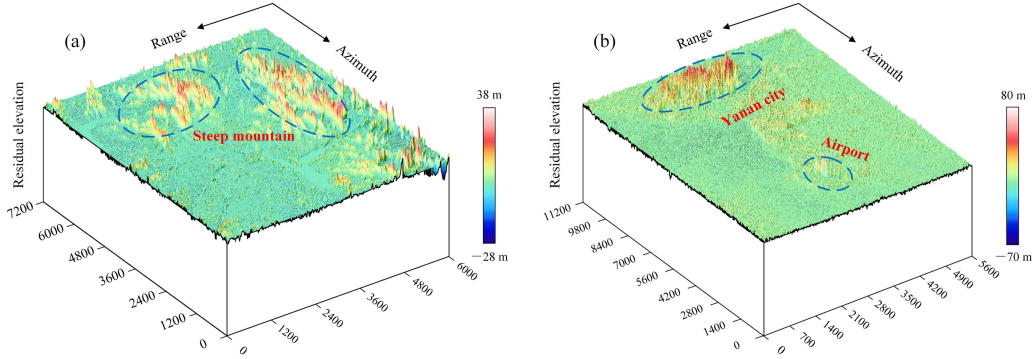


Fig. 8. Residual elevation calculated by ISCM. (a) SD area. (b) YA area.

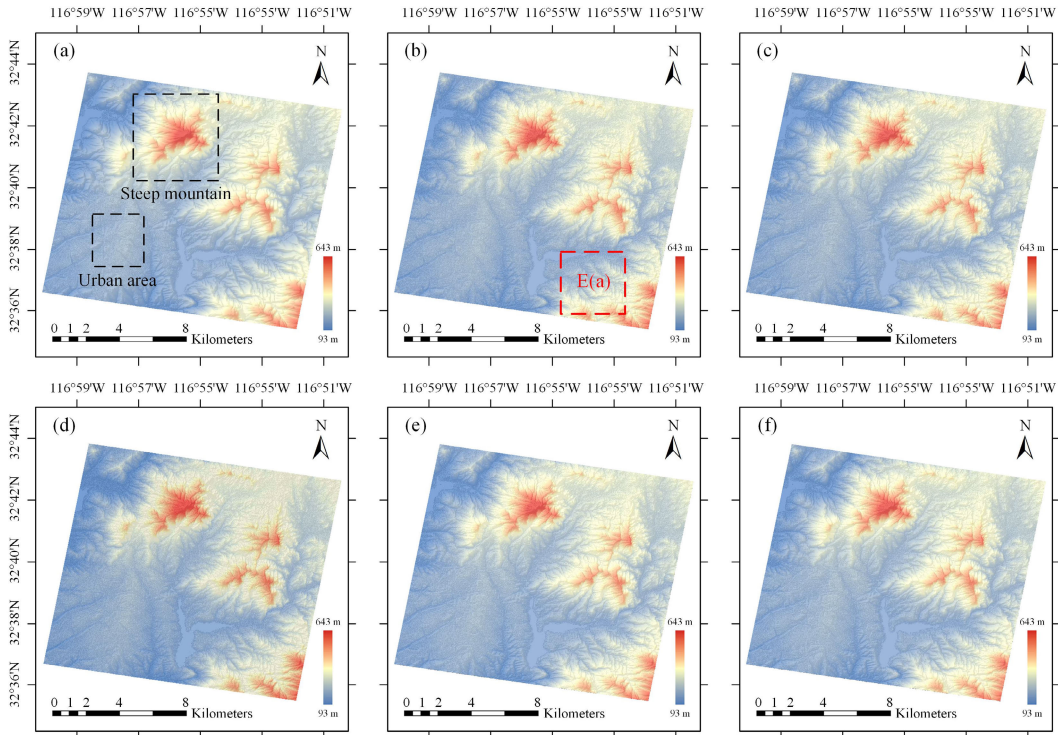


Fig. 9. DEM generated for the SD area. (a) ALOS 12.5-m DEM. (b) LM 3-m DEM. (c) PM 3-m DEM. (d) PSI 3-m DEM. (e) LM + IS 3-m DEM. (f) ISCM 3-m DEM.

The accuracies of the DEMs produced by the different SAR methods and the photogrammetric DEMs were further analyzed using E_{\max} , RMSE, MAE, and LE90. The results show a significant improvement in DEM accuracy after applying the ISCM methods. Tables II and III illustrate the advantages of the DEMs produced by the ISCM method over the traditional LM, SM, PM, and PSI methods. For the SD area, the RMSEs of the DEMs produced by LM + IS and ISCM with the photogrammetric DEMs are 3.62 and 3.20 m, with an improvement of 18.1%–34.7% and 30.8%–44.9% respectively, compared to the traditional MB-InSAR method. For the YA area, the RMSEs of the DEMs are 4.79 and 4.41 m, with an improvement of 15.2%–33.1% and 21.9%–38.4% respectively. These results demonstrate the feasibility of the proposed method for atmospheric noise and other residual signals removal and ISCM during SAR DEM

TABLE II
COMPARISON OF ELEVATION ACCURACY INDEXES FOR SD (UNIT: m)

Indexes	E_{\max}	RMSE	MAE	LE90
LM	22.05	5.63	5.40	9.22
SM	21.51	5.81	5.26	9.80
PM	21.15	5.68	5.09	9.57
LM+GACOS	20.69	4.66	4.92	8.07
PSI	20.20	4.63	5.01	7.68
LM+IS	18.67	3.79	4.19	7.18
LM+IS+BC	18.48	3.62	3.95	7.09
ISCM	17.73	3.20	3.63	6.77

generation. The ISCM has successfully improved the quality of the generated DEMs so that the vertical accuracy LE90 is about 6.77 m for SD and 8.65 m for YA, which can meet the US HRTI-3 standard [51].

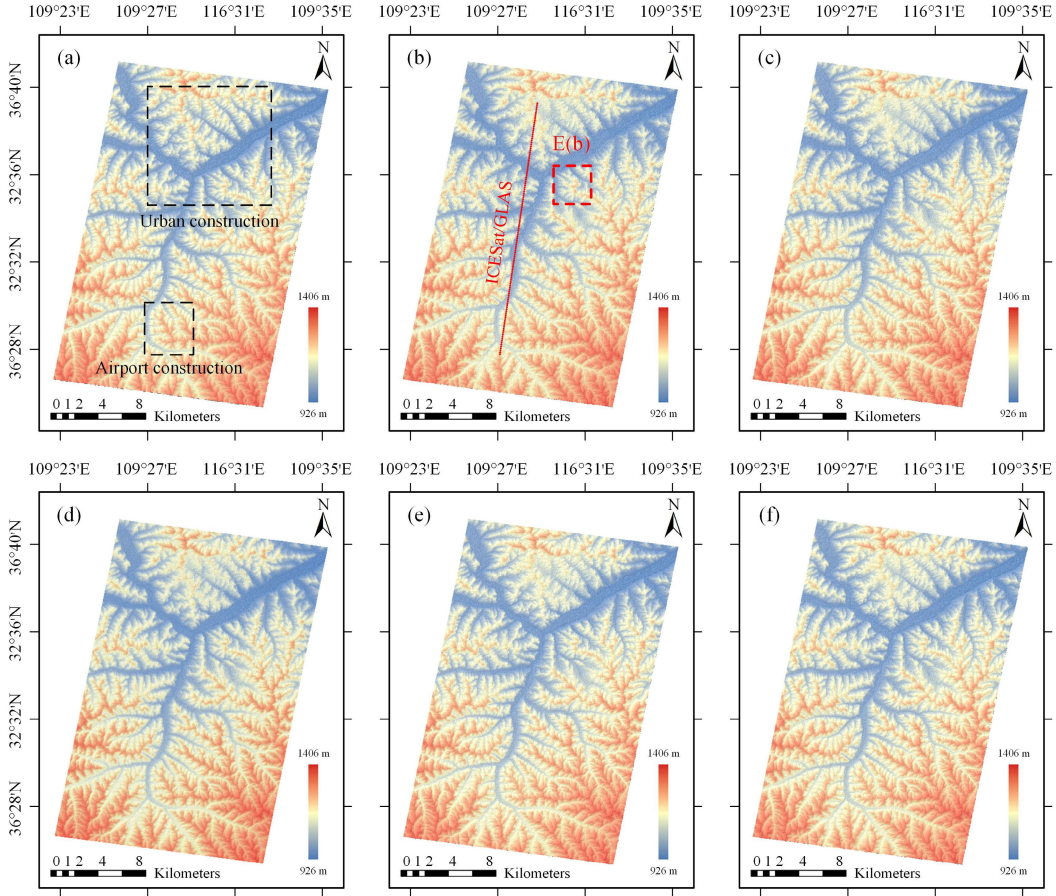


Fig. 10. DEM generated for the YA area. (a) ALOS 12.5-m DEM. (b) LM 6-m DEM. (c) PM 6-m DEM. (d) PSI 6-m DEM. (e) LM + IS 6-m DEM. (f) ISCM 6-m DEM.

TABLE III

COMPARISON OF ELEVATION ACCURACY INDEXES FOR YA (UNIT: m)

Indexes	E_{\max}	RMSE	MAE	LE90
LM	35.33	6.51	5.93	9.39
SM	34.93	7.17	6.97	10.48
PM	33.31	7.09	7.05	10.52
LM+GACOS	31.82	6.69	6.76	10.31
PSI	31.84	5.65	5.56	9.51
LM+IS	29.38	4.79	4.88	8.93
LM+IS+BC	28.21	4.60	4.71	8.80
ISCM	27.11	4.41	4.59	8.65

From Tables II and III, we can see that the overall accuracy of the SD area is higher than that of the YA area, and the main reasons are that the data acquired in the SD area are TerraSAR-X Stripmap mode data with 3-m resolution, while the data acquired in the YA area are stripmap dual-mode data with 6-m resolution. The overall accuracy of the SD area is better than that of the YA area at the sensor resolution. However, due to the different resolutions of the collected data sensors themselves, the performance of the sensors needs to be further investigated by collecting SAR satellite data at the same resolution.

2) *Accuracy Evaluation Using ICESat/GLAS Elevation Data:* To further validate the accuracy of the ISCM method for DEM generation, 128 ICESat/GLAS data were collected from

the YA area, as shown in Fig. 10. Considering the difference in resolution between the ICESat/GLAS data (about 65 m in diameter) and the DEMs generated by the ISCM (about 6 m in the YA area), we compared the elevation value from a 9×9 window in the YA area with the elevation of the GLAS points [16]. The ICESat/GLAS elevation measurements were compared with the center position (H1), minimum (H2), maximum (H3), and average (H4) values of the different DEM generation methods within the corresponding 9×9 geographical window. Table IV shows the mean difference and RMSE of the different DEMs with ICESat/GLAS. The RMSE is significantly improved in H1–H4, with improvements of 16.9%–30.0%, 25.0%–28.5%, 19.2%–30.8%, and 13.7%–29.5% compared to the traditional MB-InSAR method, respectively. In addition, the variability of H1–H4 is relatively small, thus demonstrating the accuracy of the geographic location of the SAR-generated DEMs.

3) *Accuracy Evaluation for ISCM Modeling Using Residual Phase:* To analyze the accuracy of the InSAR modeling considering linear deformation, seasonal deformation, and environmental factors, using the residual phase to validate the InSAR modeling [30]. A smaller residual phase indicates a better performance of the InSAR modeling in generating DEMs and deformations. Fig. 13 shows the residual phases of the 36 selected interferograms in the SD area and the 34 selected interferograms selected in the YA area.

TABLE IV
MEAN DIFFERENCE AND RMSE OF DIFFERENT DEMS WITH ICESAT/GLAS (UNIT: m)

Different methods	H1		H2		H3		H4	
	Mean	RMSE	Mean	RMSE	Mean	RMSE	Mean	RMSE
LM	-1.28	6.95	-0.07	6.49	-2.44	7.26	-1.24	6.84
SM	-1.06	5.99	-0.01	5.80	-1.97	6.22	-0.98	5.85
PM	-1.28	6.89	-0.19	6.54	-2.29	7.03	-1.25	6.77
LM+GACOS	-1.21	5.87	-0.19	6.23	-2.14	6.35	-1.16	5.78
PSI	-1.14	5.85	-0.26	6.29	-2.26	6.27	-1.22	5.59
LM+IS	-1.09	5.57	-0.32	5.28	-1.83	5.69	-1.07	5.45
LM+IS+BC	-1.07	5.07	-0.30	4.87	-1.68	5.24	-0.98	5.03
ISCM	-1.02	4.86	-0.29	4.67	-1.58	5.02	-0.93	4.82

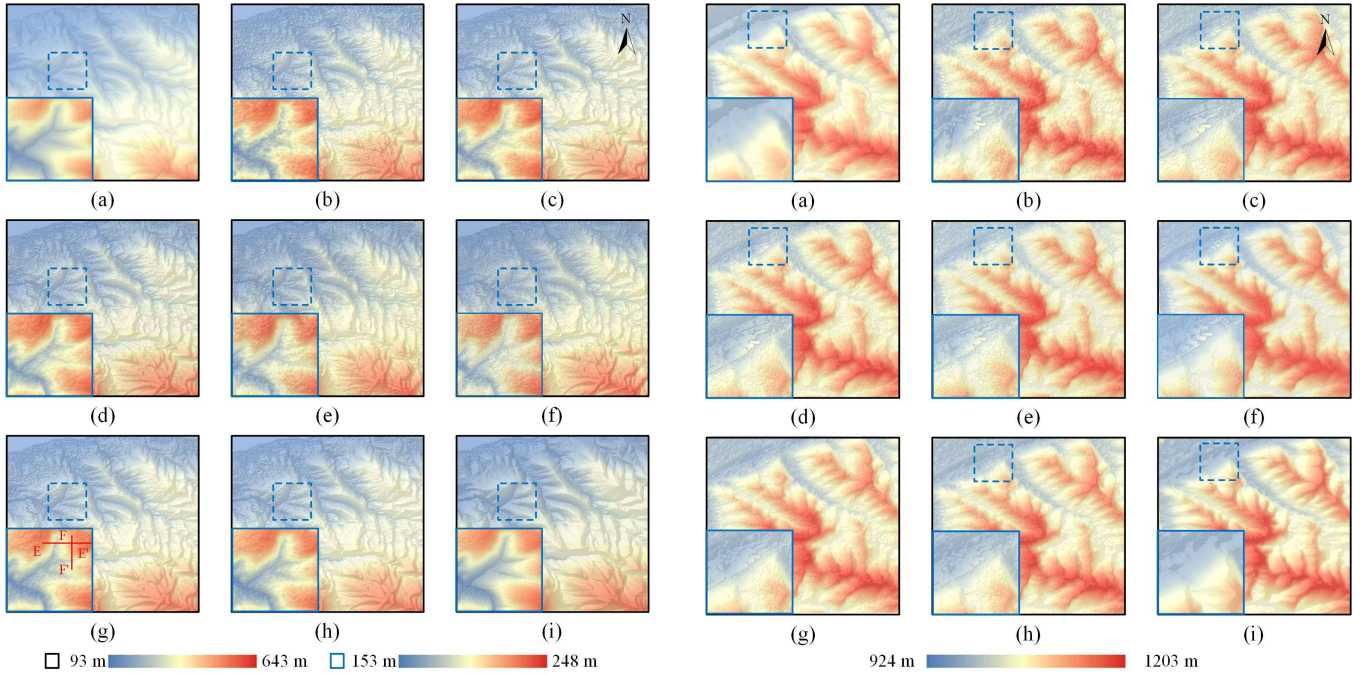


Fig. 11. Comparison between different DEM generation methods for the SD area. (a) ALOS 12.5-m DEM. (b) LM 3-m DEM. (c) SM 3-m DEM. (d) PM 3-m DEM. (e) LM + GACOS 3-m DEM. (f) PSI 3-m DEM. (g) LM + IS 3-m DEM. (h) ISCM 3-m DEM. (i) Photogrammetric DEM.

The residual phases obtained by the ISCM method are significantly lower than those obtained by the traditional method. By calculating the STD of the residual phase, for the SD area, the STD of the traditional LM model is ± 0.23 rad, while that of ISCM is ± 0.16 rad, with an improvement of 30.4%; for the YA area, the STD of the traditional LM model is ± 0.21 rad, while that of the ISCM is ± 0.13 rad, with an improvement of 38.0%. These results confirm the feasibility and reliability of the InSAR model proposed in this study for DEM generation.

4) Accuracy Evaluation for Deformation Using GNSS Data:
To validate the ability of the ISCM to capture the deformation, two GNSS points in the SD area (G1 and G2 in Fig. 6) were collected for further evaluation [52]. It should be noted that G1 points are used for accurate verification of deformation over the same period. Due to limitations in the collection of historical GNSS data, G2 points are only used to assess the consistency of deformation trends. Fig. 14 shows the

Fig. 12. Comparison between different DEM generation methods for the YA area. (a) ALOS 12.5-m DEM. (b) LM 6-m DEM. (c) SM 6-m DEM. (d) PM 6-m DEM. (e) LM + GACOS 6-m DEM. (f) PSI 6-m DEM. (g) LM + IS 6-m DEM. (h) ISCM 6-m DEM. (i) Photogrammetric DEM.

comparison of time series deformation between different methods and GNSS. The RMSEs between the ISCM and GNSS are ± 2.79 and ± 4.66 mm in G1 and G2, respectively, while the LMs are ± 7.48 and ± 9.97 mm. In addition, from Fig. 14, the time series of the ISCM model are consistent with GNSS and can better capture the nonlinear deformation of the surface, indicating that the ISCM model has good potential for deformation modeling.

IV. DISCUSSION

A. Analysis of the DEM Applications for Terrain Feature Identification

To further analyze the effect of ISCM on DEM generation, the DEMs of area E(a) for the SD area were selected and used for slope, aspect, and river network generation, the sample as shown in Figs. 15–17.

The differences observed in the extracted slope, aspect, and river network of the different methods compared to

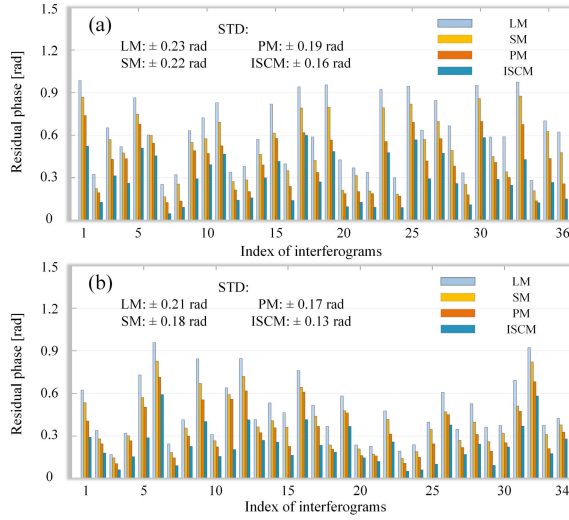


Fig. 13. Residual phases of DEMs generated by different methods. (a) SD area. (b) YA area.

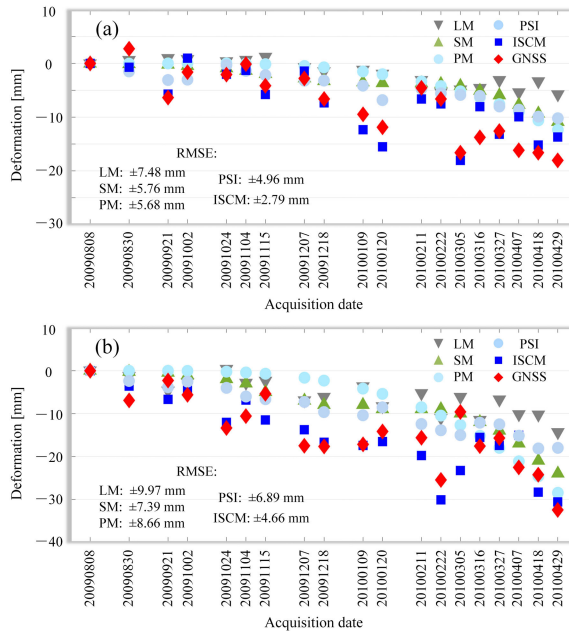


Fig. 14. Comparison of time series deformation between different methods and GNSS for the SD area. (a) G1 point. (b) G2 point.

photogrammetric DEMs reflect their respective abilities to preserve topographic features. The better preservation of terrain features in the generated DEM demonstrates the superior quality of the resulting DEM product. It can be seen from Figs. 15 and 16 that the traditional LM, SM, and PM methods can produce more refined terrain features compared to the photogrammetric DEMs, but the retention of terrain features is weak due to a variety of factors such as atmospheric and noise, other residual signals, and deformation errors. In contrast, the terrain features produced by ISCM are more consistent with the terrain features of the photogrammetric DEM. In addition, the surface details of the DEM products are clearer and more representative of the rich topographic features. From Fig. 17, we performed hydrological analyses on

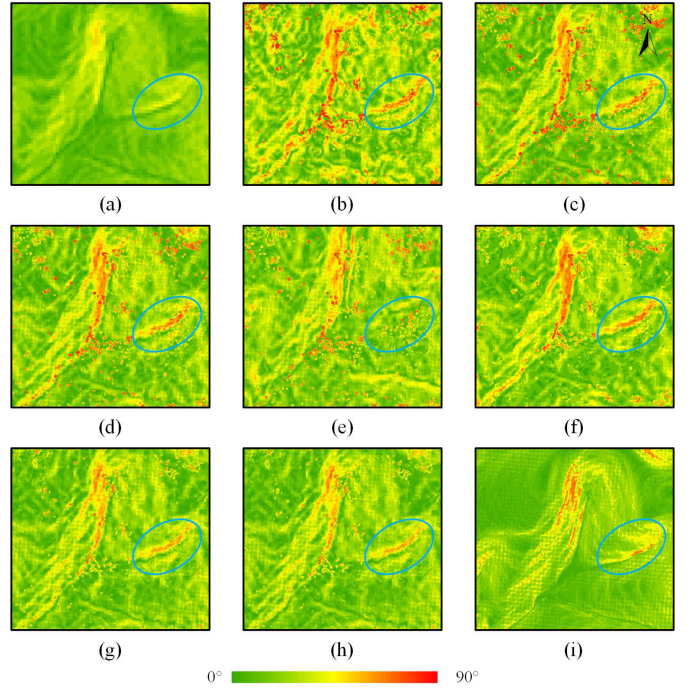


Fig. 15. Sample slope maps based on DEMs generated by different methods. (a) ALOS 12.5-m slope. (b) LM 3-m slope. (c) SM 3-m slope. (d) PM 3-m slope. (e) LM + GACOS 3-m slope. (f) PSI 3-m slope. (g) LM + IS 3-m slope. (h) ISCM 3-m slope. (i) Photogrammetric slope.

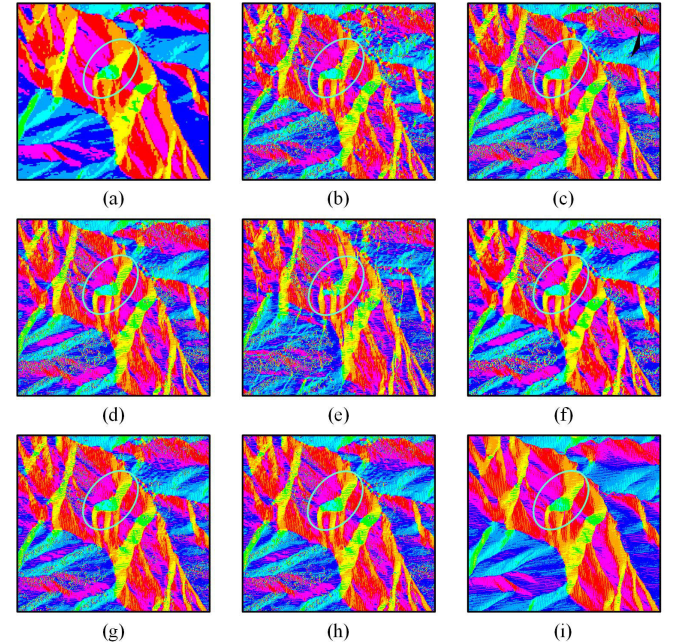


Fig. 16. Sample aspect maps based on DEMs generated by different methods. (a) ALOS 12.5-m aspect. (b) LM 3-m aspect. (c) SM 3-m aspect. (d) PM 3-m aspect. (e) LM + GACOS 3-m aspect. (f) PSI 3-m aspect. (g) LM + IS 3-m aspect. (h) ISCM 3-m aspect. (i) Photogrammetric aspect.

the DEM-generated river network, the river networks derived from the ALOS DEM appear relatively simple, while the InSAR and photogrammetric river networks show more detail.

To validate the performance of the terrain features, we performed an analysis of slope and aspect and compared

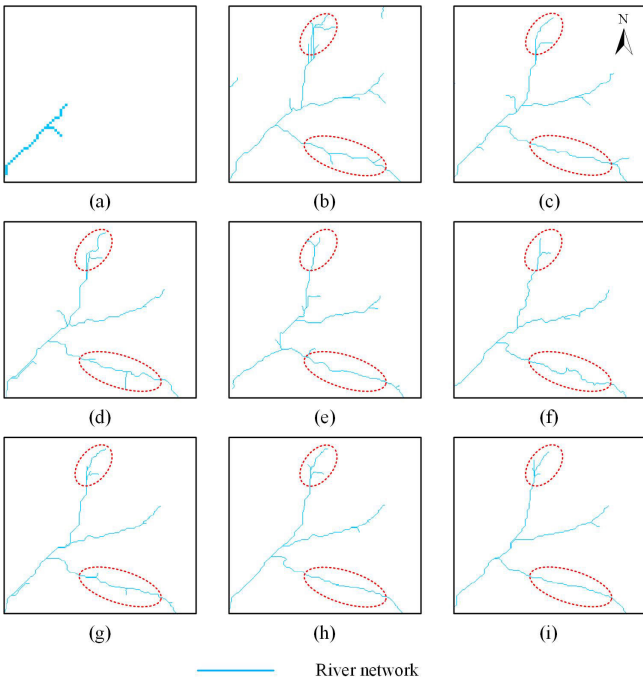


Fig. 17. Sample river network maps based on DEMs generated by different methods. (a) ALOS 12.5-m river network. (b) LM 3-m river network. (c) SM 3-m river network. (d) PM 3-m river network. (e) LM + GACOS 3-m river network. (f) PSI 3-m river network. (g) LM + IS 3-m river network. (h) ISCM 3-m river network. (i) Photogrammetric river network.

TABLE V
COMPARISON OF TERRAIN FEATURES INDEXES (UNIT: $^{\circ}$)

Indexes	LM	SM	PM	PSI	LM+IS	ISCM
E_{Slope}	7.64	6.84	6.78	6.17	5.54	5.52
E_{Aspect}	19.08	17.37	17.41	17.22	16.51	16.02

the results with those obtained from the photogrammetric DEM. Table V shows the MAE of slope E_{Slope} and aspect E_{Aspect} performance of DEMs generated by different methods with the photogrammetric DEM, and the results show differences in the ability of different methods to capture terrain features. Furthermore, the capture of terrain features gradually improves as factors such as atmospheric noise, other residual signals, and deformation error are optimized. In particular, the proposed ISCM method shows improvements of 10.5%–27.7% and 7.0%–16.0% in slope and aspect representation, respectively, compared to the traditional MB-InSAR method.

B. Analysis of the Horizontal and Vertical Profiles

To illustrate the differences between the DEMs produced by the different methods, the horizontal profile EE' and the vertical profile FF' from Fig. 11(e) are selected for further analysis. From Fig. 18, it can be seen that although the traditional LM, SM, and PM methods are capable of reproducing rich topographic information (the surface undulation is much more detailed), they are subject to atmospheric and noise effects, baseline and deformation

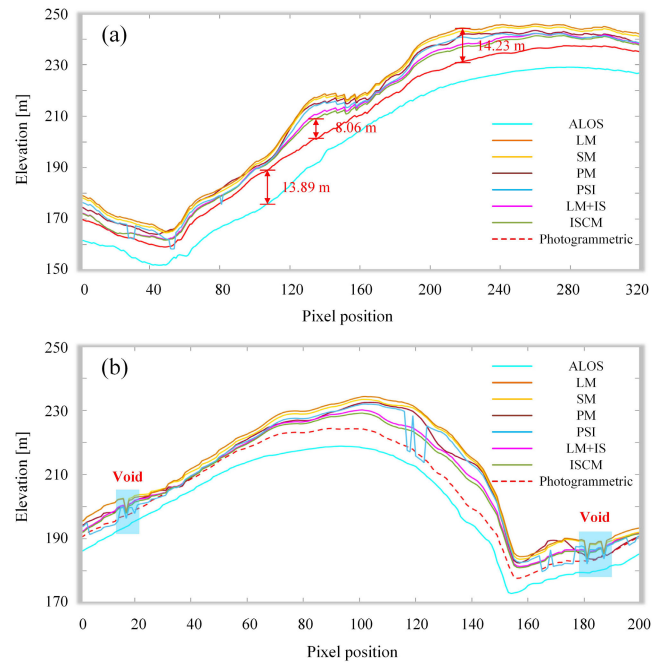


Fig. 18. Comparison between different DEMs using the horizontal and vertical profiles. (a) Horizontal profile EE'. (b) Horizontal profile FF'.

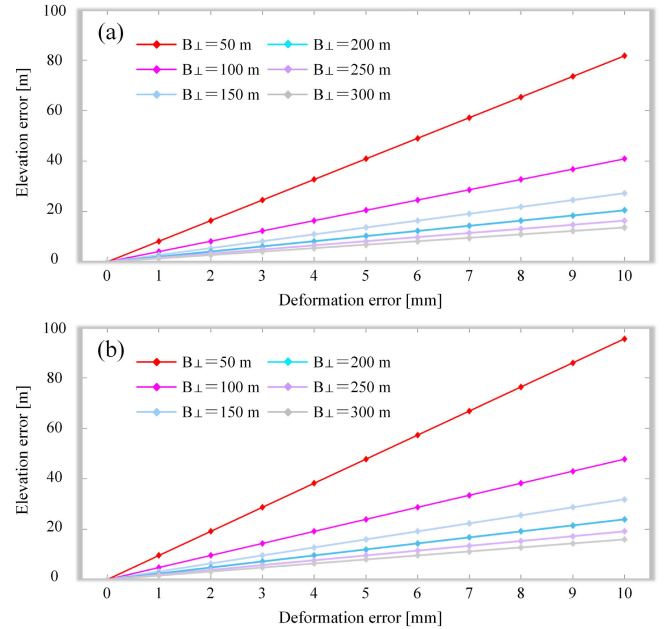


Fig. 19. Influence of deformation errors on elevation measurements. (a) SD area. (b) YA area.

modeling errors, and other factors that are significantly different from the photogrammetric DEM profiles.

From the horizontal profile EE', the maximum difference between the LM method and the photogrammetric DEM is 14.23 m, while the maximum difference between the ISCM method and the photogrammetric DEM is only 8.06 m. The traditional SAR method has limitations in producing DEMs due to spatial-temporal incoherence or geometric distortions caused by layover and shadows, and the DEMs produced by the ISCM method are better able to compensate for this

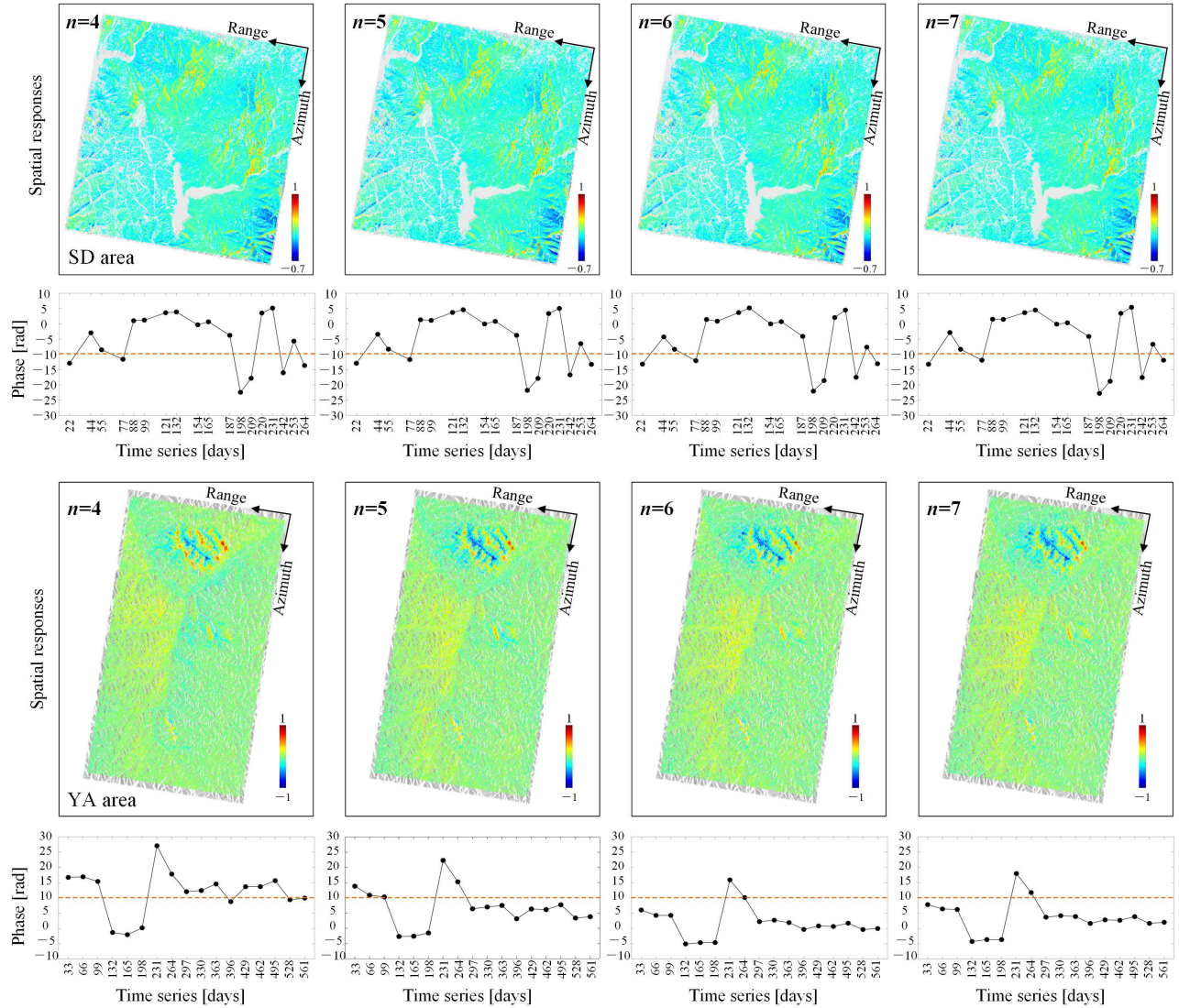


Fig. 20. Effect of separation number on topography phases.

phenomenon. However, it is worth noting that the interpolated fusion approach still has some limitations in some void areas, as shown in Fig. 18(b), and this phenomenon of erroneous artifacts needs to be further improved.

C. Analysis of the Influence of Deformation Errors on Elevation Measurements

To test how the phase contribution of deformation errors affects the resulting DEM accuracy. Satellite parameters in the SD and YA areas were used to test the effect of 0–10-mm deformation errors on elevation measurements under different perpendicular baselines, as shown in Fig. 19. Fig. 19 shows that for a larger perpendicular baseline of 300 m, a deformation error of 10 mm can cause an elevation error of 13.62 and 15.92 m in the SD and YA areas, respectively. Also, for a small perpendicular baseline of 50 m, a deformation error of 10 mm can cause an elevation error of 81.73 and 95.54 m. Therefore, if the deformation phase cannot be accurately separated or modeled, the error is introduced into the DEM and is a major source of error in DEM reconstruction.

D. Analysis of the Effect of Separation Number on Topography Phases

The number of independent component separations is crucial for the accurate separation of the signals, so we tested the effect on the spatial response and time series of the topography phase when the number of separations was 4, 5, 6, and 7. From Fig. 20, the time series and spatial response of the topography phase in the SD area are relatively stable. However, there is a large variability in the YA area. We suspect that the reason for this is that the correlation between the deformation and topography phase in the SD area is small, and the topography phase is relatively stable for different numbers of separations. On the other hand, the deformation and topography phase in the YA area have a larger correlation. In this case, the deformation and topography phases are entangled. Therefore, the combination of deformation and topography phase as a whole in this article to obtain the residual elevation efficiently and robustly.

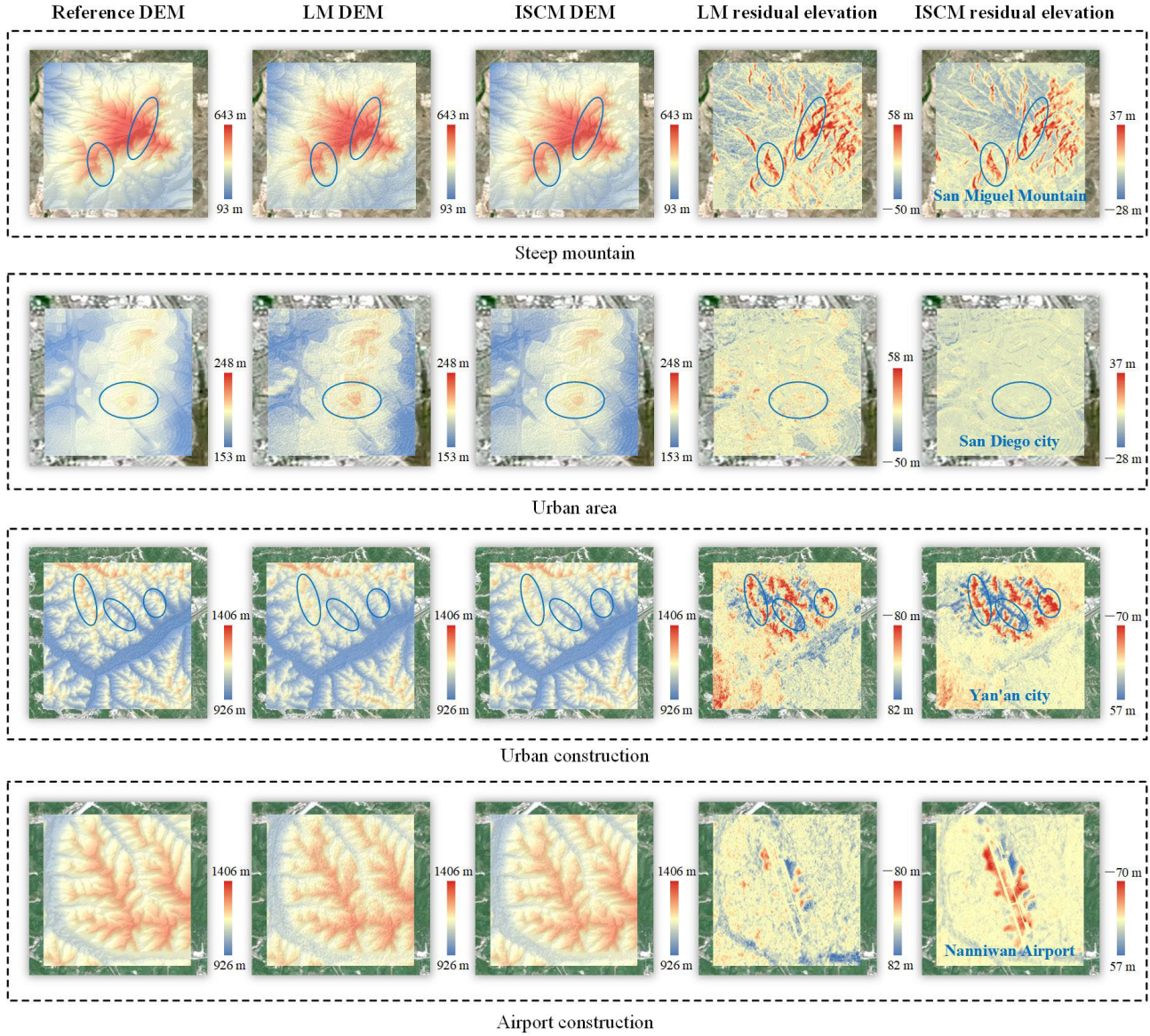


Fig. 21. Response of the ISCM to different terrain surfaces (i.e., conditions).

E. Analysis of the Response of the ISCM to Different Terrain

During the DEM generation process using the ISCM method, we found that the residual elevation responds differently to different terrain surfaces, as shown in Fig. 8. The residual elevation generated by ISCM shows more significant variations in areas with steep mountainous terrain, while it is relatively smaller in flat areas. This difference can be attributed to the influence of the reference DEM used, which has a larger error in mountainous areas and a smaller error in flat areas. It also seems to be simply related to the different resolution classes and different viewing geometries of the TerraSAR-X data in the SD area and the PAZ data in the YA area with the ALOS 12.5-m DEM. The HR DEM generated in this study effectively recovers the terrain details and thus compensates for the errors in the reference DEM.

To further explore the response of the ISCM to different terrains, the DEMs of different scenes (as shown in

Figs. 9 and 10) were selected for comparison. From Fig. 21, the ISCM DEM shows richer terrain details than the LM DEM. In terms of residual elevation, the ISCM has less noise and clearer topography, reflecting the potential advantages of the ISCM in improving atmospheric noise, other residual signals, and deformation modeling errors. For the SD area of the steep mountains, the DEMs generated by ISCM show better recovery of the steep ridges and are consistent with the textural characteristics of the San Diego Mountains. This indicates that the ISCM is effective in capturing the detailed terrain features of rugged landscapes; the ISCM provides a finer representation of the urban surface features of San Diego and can capture subtle changes in urban topography.

In addition, for the YA area of the urban construction and the airport construction, the ISCM better reflects the correction for surface changes. The residual elevation in Yan'an city and its airport is particularly noticeable, and according to the geographic survey of Yan'an city, we found that the

main reason is that the PAZ data used in the experiment were from 2022 to 2023, while the reference ALOS DEM was collected in 2008. The temporal change of the city of Yan'an and its airport is a well-known result of the extensive excavation and filling activities in recent years. According to the investigation, the government proposed the Mountain Excavation and City Construction (MECC) project in December 2011, and it was reported to have started in April 2012 [53]. The Yan'an Nanniwan Airport was constructed in July 2013 and officially opened to traffic in November 2018. The topographical and geological conditions of the Loess Plateau Wet Trapped Loess Area are complicated by high excavation and deep filling with incongruent deformation (the maximum filling depth is nearly 100 m). In addition to the abovementioned effect of the mountainous area, the effect of urban construction and airport construction on the topography of Yan'an City also contributes significantly to this phenomenon. The ISCM residual elevations are highly consistent with the spatial distribution and magnitude, and the difference between TanDEM-X DEM and SRTM [54]. Overall, the ISCM method demonstrates its effectiveness in capturing terrain variations and accurately representing the changes caused by different terrain surfaces (i.e., conditions), including steep mountains, urban construction, and airport development.

V. CONCLUSION

To compensate for the limitations of atmospheric noise, other residual signals, and inaccurate deformation modeling in the MB-InSAR DEM generation, the spatial ICA phase separation and ISCM method was proposed in this article. TerraSAR-X and PAZ data were acquired in the SD and YA areas for the test. The accuracy of the DEMs produced by the ISCM was verified using photogrammetric DEM and ICESat/GLAS elevation data. The main conclusions are as follows.

First, compared to the traditional LM, SM, PM, and PSI methods, the ISCM method can significantly improve the effects of atmospheric noise, other residual signals, and deformation error in the DEM generation. The accuracy of the generated DEM can be improved by 30.8%–44.9% in the SD area and 21.9%–38.4% in the YA area. In addition, the modeling error analysis shows that the ISCM has a high modeling accuracy.

Second, the DEMs generated by the ISCM method have significant advantages in generating slope, aspect, and river networks and can show the texture and detail of features more clearly, with better preservation of terrain features.

Third, the DEMs generated by the ISCM method provide a better representation of the terrain in different scenes, especially for the terrain changes caused by steep mountains, urban construction, and airport construction. The DEMs can more clearly reflect the basic features of the terrain and geomorphology, confirming that the ISCM is more meaningful in recovering the DEM changes caused by the long time series surface construction.

This article still has some limitations that need further investigation. 1) the method only analyzes and improves the

errors in MB-InSAR DEM generation and the spatial-temporal incoherence or layover and shadow problems of InSAR can only be overcome by simple interpolation fusion and 2) the interferometric pairs need large spatial baselines in mountainous areas, which could lead to decorrelation problems and unwrapping errors. In future research, we will address this limitation by using artificial intelligence (AI) fusion combined with ascending and descending data.

ACKNOWLEDGMENT

The TerraSAR-X and PAZ satellite images used in this work were provided by the DLR and ESA (Dara Order Program Project: MTH3930, PP0092621, and PP0092940). The ICESat/GLAS data were freely available from the NASA Distributed Active Archive Center (DAAC) at the National Snow and Ice Data Center (NSIDC).

REFERENCES

- [1] Y. Chen et al., "The simulation of surface flow dynamics using a flow-path network model," *Int. J. Geographical Inf. Sci.*, vol. 28, no. 11, pp. 2242–2260, May 2014, doi: [10.1080/13658816.2014.917312](https://doi.org/10.1080/13658816.2014.917312).
- [2] T. H. Tarekegn, A. T. Haile, T. Rientjes, P. Reggiani, and D. Alkema, "Assessment of an ASTER-generated DEM for 2D hydrodynamic flood modeling," *Int. J. Appl. Earth Observ. Geoinformation*, vol. 12, no. 6, pp. 457–465, Dec. 2010, doi: [10.1016/j.jag.2010.05.007](https://doi.org/10.1016/j.jag.2010.05.007).
- [3] Z. Yang, Q. Zhang, X. Ding, and W. Chen, "Analysis of the quality of daily DEM generation with geosynchronous InSAR," *Engineering*, vol. 6, no. 8, pp. 913–918, Aug. 2020, doi: [10.1016/j.eng.2020.07.003](https://doi.org/10.1016/j.eng.2020.07.003).
- [4] A. Zhou, Y. Chen, J. P. Wilson, G. Chen, W. Min, and R. Xu, "A multi-terrain feature-based deep convolutional neural network for constructing super-resolution DEMs," *Int. J. Appl. Earth Observ. Geoinformation*, vol. 120, Jun. 2023, Art. no. 103338, doi: [10.1016/j.jag.2023.103338](https://doi.org/10.1016/j.jag.2023.103338).
- [5] B. Rabus, M. Eineder, A. Roth, and R. Bamler, "The shuttle radar topography mission—A new class of digital elevation models acquired by spaceborne radar," *ISPRS J. Photogramm. Remote Sens.*, vol. 57, no. 4, pp. 241–262, Feb. 2003, doi: [10.1016/s0924-2716\(02\)00124-7](https://doi.org/10.1016/s0924-2716(02)00124-7).
- [6] T. Podobnikar, "Production of integrated digital terrain model from multiple datasets of different quality," *Int. J. Geographical Inf. Sci.*, vol. 19, no. 1, pp. 69–89, Jan. 2005, doi: [10.1080/13658810412331280130](https://doi.org/10.1080/13658810412331280130).
- [7] Z. Li, W. Zhu, C. Yu, Q. Zhang, and Y. Yang, "Development status and trends of imaging geodesy," *Acta Geodaetica et Cartographica Sinica*, vol. 52, no. 11, pp. 1805–1834, Nov. 2023, doi: [10.11947/j.AGCS.2023.20230003](https://doi.org/10.11947/j.AGCS.2023.20230003).
- [8] T. Toutin and L. Gray, "State-of-the-art of elevation extraction from satellite SAR data," *ISPRS J. Photogramm. Remote Sens.*, vol. 55, no. 1, pp. 13–33, Feb. 2000, doi: [10.1016/s0924-2716\(99\)00039-8](https://doi.org/10.1016/s0924-2716(99)00039-8).
- [9] R. F. Hanssen, *Radar Interferometry: Data Interpretation and Error Analysis*. Alphen aan den Rijn, The Netherlands: Kluwer, 2001.
- [10] P. Berardino, G. Fornaro, R. Lanari, and E. Sansosti, "A new algorithm for surface deformation monitoring based on small baseline differential SAR interferograms," *IEEE Trans. Geosci. Remote Sens.*, vol. 40, no. 11, pp. 2375–2383, Nov. 2002, doi: [10.1109/TGRS.2002.803792](https://doi.org/10.1109/TGRS.2002.803792).
- [11] S. Samsonov, M. van der Kooij, and K. Tiampo, "A simultaneous inversion for deformation rates and topographic errors of DInSAR data utilizing linear least square inversion technique," *Comput. Geosci.*, vol. 37, no. 8, pp. 1083–1091, Aug. 2011, doi: [10.1016/j.cageo.2011.01.007](https://doi.org/10.1016/j.cageo.2011.01.007).
- [12] C. Zhao, F. Qu, Q. Zhang, and W. Zhu, "A combined multi-interferogram algorithm for high resolution DEM reconstruction over deformed regions with TerraSAR-X data," *J. Geodynamics*, vol. 61, pp. 148–153, Oct. 2012, doi: [10.1016/j.jog.2012.04.004](https://doi.org/10.1016/j.jog.2012.04.004).
- [13] H. Fattah and F. Amelung, "DEM error correction in InSAR time series," *IEEE Trans. Geosci. Remote Sens.*, vol. 51, no. 7, pp. 4249–4259, Jul. 2013, doi: [10.1109/TGRS.2012.2227761](https://doi.org/10.1109/TGRS.2012.2227761).
- [14] W. Zhang et al., "Improved DEM reconstruction method based on multibaseline InSAR," *IEEE Geosci. Remote Sens. Lett.*, vol. 19, pp. 1–5, Apr. 2022, doi: [10.1109/LGRS.2021.3069239](https://doi.org/10.1109/LGRS.2021.3069239).

- [15] M. Lachaise, T. Fritz, and R. Bamler, "The dual-baseline phase unwrapping correction framework for the TanDEM-X mission Part 1: Theoretical description and algorithms," *IEEE Trans. Geosci. Remote Sens.*, vol. 56, no. 2, pp. 780–798, Feb. 2018, doi: [10.1109/TGRS.2017.2754923](https://doi.org/10.1109/TGRS.2017.2754923).
- [16] Y. Dong, L. Zhang, H. Jiang, T. Balz, and M. Liao, "Cascaded multi-baseline interferometry with bistatic TerraSAR-X/TanDEM-X observations for DEM generation," *ISPRS J. Photogramm. Remote Sens.*, vol. 171, pp. 224–237, Jan. 2021, doi: [10.1016/j.isprsjprs.2020.11.012](https://doi.org/10.1016/j.isprsjprs.2020.11.012).
- [17] X. X. Zhu, G. Baier, M. Lachaise, Y. Shi, F. Adam, and R. Bamler, "Potential and limits of non-local means InSAR filtering for TanDEM-X high-resolution DEM generation," *Remote Sens. Environ.*, vol. 218, pp. 148–161, Dec. 2018, doi: [10.1016/j.rse.2018.09.012](https://doi.org/10.1016/j.rse.2018.09.012).
- [18] M. Liao, H. Jiang, Y. Wang, T. Wang, and L. Zhang, "Improved topographic mapping through high-resolution SAR interferometry with atmospheric effect removal," *ISPRS J. Photogramm. Remote Sens.*, vol. 80, pp. 72–79, Jun. 2013, doi: [10.1016/j.isprsjprs.2013.03.008](https://doi.org/10.1016/j.isprsjprs.2013.03.008).
- [19] Z. Qiming, Z. Xiaojie, and J. Jian, "Atmospheric correction of spaceborne repeat-pass InSAR DEM generation based on WRF," *Nat. Remote Sens. Bull.*, vol. 20, no. 5, pp. 1151–1160, Jul. 2016, doi: [10.11834/jrs.20166174](https://doi.org/10.11834/jrs.20166174).
- [20] W. Peng, Q. Wang, F. B. Zhan, and Y. Cao, "Spatiotemporal ocean tidal loading in InSAR measurements determined by kinematic PPP solutions of a regional GPS network," *IEEE J. Sel. Topics Appl. Earth Observ. Remote Sens.*, vol. 13, pp. 3772–3779, Jun. 2020, doi: [10.1109/JSTARS.2020.3002777](https://doi.org/10.1109/JSTARS.2020.3002777).
- [21] Y. Du, L. Zhang, G. Feng, Z. Lu, and Q. Sun, "On the accuracy of topographic residuals retrieved by MTInSAR," *IEEE Trans. Geosci. Remote Sens.*, vol. 55, no. 2, pp. 1053–1065, Feb. 2017, doi: [10.1109/TGRS.2016.2618942](https://doi.org/10.1109/TGRS.2016.2618942).
- [22] P. Comon, "Independent component analysis, a new concept?" *Signal Process.*, vol. 36, no. 3, pp. 287–314, Apr. 1994, doi: [10.1016/0165-1684\(94\)90029-9](https://doi.org/10.1016/0165-1684(94)90029-9).
- [23] J. Chen et al., "Increased water content in the active layer revealed by regional-scale InSAR and independent component analysis on the central Qinghai-Tibet Plateau," *Geophys. Res. Lett.*, vol. 49, no. 15, pp. 1–10, Aug. 2022, doi: [10.1029/2021gl097586](https://doi.org/10.1029/2021gl097586).
- [24] X. Xing et al., "Independent component analysis (ICA) based method for estimating the deformation of highways in permafrost region (HPICA)—A case study of maduo section of Gongyu highway," *IEEE J. Sel. Topics Appl. Earth Observ. Remote Sens.*, vol. 17, pp. 970–984, 2024, doi: [10.1109/JSTARS.2023.3336916](https://doi.org/10.1109/JSTARS.2023.3336916).
- [25] M. Peng et al., "Characterization and prediction of InSAR-derived ground motion with ICA-assisted LSTM model," *Remote Sens. Environ.*, vol. 301, Feb. 2024, Art. no. 113923, doi: [10.1016/j.rse.2023.113923](https://doi.org/10.1016/j.rse.2023.113923).
- [26] H. Liang, L. Zhang, Z. Lu, and X. Li, "Nonparametric estimation of DEM error in multitemporal InSAR," *IEEE Trans. Geosci. Remote Sens.*, vol. 57, no. 12, pp. 10004–10014, Dec. 2019, doi: [10.1109/TGRS.2019.2930802](https://doi.org/10.1109/TGRS.2019.2930802).
- [27] A. Ferretti, C. Prati, and F. Rocca, "Multibaseline phase unwrapping for InSAR topography estimation," *Nuovo Cimento-Societa Italiana Di Fisica Sezione C*, vol. 24, no. 1, pp. 159–176, Feb. 2001.
- [28] D. Li, K. Z. Deng, X. X. Gao, and H. P. Niu, "Monitoring and analysis of surface subsidence in mining area based on SBAS-InSAR," *Geomatics Inf. Sci. Wuhan Univ.*, vol. 43, no. 10, pp. 1531–1537, Oct. 2018, doi: [10.13203/j.whugis20160566](https://doi.org/10.13203/j.whugis20160566).
- [29] Y. Zhang, X. Meng, C. Jordan, A. Novellino, T. Dijkstra, and G. Chen, "Investigating slow-moving landslides in the Zhouqu region of China using InSAR time series," *Landslides*, vol. 15, no. 7, pp. 1299–1315, Feb. 2018, doi: [10.1007/s10346-018-0954-8](https://doi.org/10.1007/s10346-018-0954-8).
- [30] R. Zhao, Z.-W. Li, G.-C. Feng, Q.-J. Wang, and J. Hu, "Monitoring surface deformation over permafrost with an improved SBAS-InSAR algorithm: With emphasis on climatic factors modeling," *Remote Sens. Environ.*, vol. 184, pp. 276–287, Oct. 2016, doi: [10.1016/j.rse.2016.07.019](https://doi.org/10.1016/j.rse.2016.07.019).
- [31] K. Zhu, X. Zhang, Q. Sun, H. Wang, and J. Hu, "Characterizing spatiotemporal patterns of land deformation in the Santa Ana basin, Los Angeles, from InSAR time series and independent component analysis," *Remote Sens.*, vol. 14, no. 11, p. 2624, May 2022, doi: [10.3390/rs14112624](https://doi.org/10.3390/rs14112624).
- [32] G. Zhang and Y. Z. Zheng, "Optimization estimation for spaceborne InSAR baseline using quadratic polynomial," *J. Appl. Sci.*, vol. 32, no. 4, pp. 409–415, doi: [10.3969/j.issn.0255-8297.2014.04.011](https://doi.org/10.3969/j.issn.0255-8297.2014.04.011).
- [33] F. Gan, G. Ruan, and J. Mo, "Baseline correction by improved iterative polynomial fitting with automatic threshold," *Chemometric Intell. Lab. Syst.*, vol. 82, nos. 1–2, pp. 59–65, May 2006, doi: [10.1016/j.chemolab.2005.08.009](https://doi.org/10.1016/j.chemolab.2005.08.009).
- [34] J. Hueso González et al., "Bistatic system and baseline calibration in TanDEM-X to ensure the global digital elevation model quality," *ISPRS J. Photogramm. Remote Sens.*, vol. 73, pp. 3–11, Sep. 2012, doi: [10.1016/j.isprsjprs.2012.05.008](https://doi.org/10.1016/j.isprsjprs.2012.05.008).
- [35] S. S. Li, Z. W. Li, J. Hu, Q. Sun, and X. Y. Yu, "Investigation of the seasonal oscillation of the permafrost over Qinghai-Tibet Plateau with SBAS-InSAR algorithm," *Chin. J. Geophys.*, vol. 56, no. 5, pp. 1476–1486, May 2013, doi: [10.6038/cjg20130506](https://doi.org/10.6038/cjg20130506).
- [36] X. Xing, H.-C. Chang, L. Chen, J. Zhang, Z. Yuan, and Z. Shi, "Radar interferometry time series to investigate deformation of soft clay subgrade settlement—A case study of Lungui highway, China," *Remote Sens.*, vol. 11, no. 4, p. 429, Feb. 2019, doi: [10.3390/rs11040429](https://doi.org/10.3390/rs11040429).
- [37] Y.-S. Xu, L. Ma, Y.-J. Du, and S.-L. Shen, "Analysis of urbanisation-induced land subsidence in Shanghai," *Natural Hazards*, vol. 63, no. 2, pp. 1255–1267, May 2012, doi: [10.1007/s11069-012-0220-7](https://doi.org/10.1007/s11069-012-0220-7).
- [38] C. Zhou et al., "InSAR time-series analysis of land subsidence under different land use types in the eastern Beijing plain, China," *Remote Sens.*, vol. 9, no. 4, p. 380, Apr. 2017, doi: [10.3390/rs9040380](https://doi.org/10.3390/rs9040380).
- [39] G. Chen, Y. Chen, J. P. Wilson, A. Zhou, Y. Chen, and H. Su, "An enhanced residual feature fusion network integrated with a terrain weight module for digital elevation model super-resolution," *Remote Sens.*, vol. 15, no. 4, p. 1038, Feb. 2023, doi: [10.3390/rs15041038](https://doi.org/10.3390/rs15041038).
- [40] A. Hooper, H. Zebker, P. Segall, and B. Kampes, "A new method for measuring deformation on volcanoes and other natural terrains using InSAR persistent scatterers," *Geophys. Res. Lett.*, vol. 31, no. 23, pp. 1–5, Dec. 2004, doi: [10.1029/2004GL021737](https://doi.org/10.1029/2004GL021737).
- [41] D. H. T. Minh and S. Tebaldini, "Interferometric phase linking: Algorithm, application, and perspective," *IEEE Geosci. Remote Sens. Mag.*, vol. 11, no. 3, pp. 46–62, Sep. 2023, doi: [10.1109/MGRS.2023.3300974](https://doi.org/10.1109/MGRS.2023.3300974).
- [42] Z. F. Yang, Z. W. Li, J. J. Zhu, J. Hu, Y. J. Wang, and G. L. Chen, "InSAR-based model parameter estimation of probability integral method and its application for predicting mining-induced horizontal and vertical displacements," *IEEE Trans. Geosci. Remote Sens.*, vol. 54, no. 8, pp. 4818–4832, Aug. 2016, doi: [10.1109/TGRS.2016.2551779](https://doi.org/10.1109/TGRS.2016.2551779).
- [43] L. J. Zhu, X. M. Xing, Y. K. Zhu, Z. H. Yuan, and Q. Xia, "An advanced time-series InSAR approach based on Poisson curve for soft clay highway deformation monitoring," *IEEE J. Sel. Topics Appl. Earth Observ. Remote Sens.*, vol. 14, pp. 7682–7698, 2021, doi: [10.1109/JSTARS.2021.3100086](https://doi.org/10.1109/JSTARS.2021.3100086).
- [44] A. Das, R. Agrawal, and S. Mohan, "Topographic correction of ALOS-PALSAR images using InSAR-derived DEM," *Geocarto Int.*, vol. 30, no. 2, pp. 145–153, Feb. 2014, doi: [10.1080/10106049.2014.883436](https://doi.org/10.1080/10106049.2014.883436).
- [45] Q. Wang et al., "Investigation of the ground displacement in Saint Petersburg, Russia, using multiple-track differential synthetic aperture radar interferometry," *Int. J. Appl. Earth Observ. Geoinf.*, vol. 87, May 2020, Art. no. 102050, doi: [10.1016/j.jag.2020.102050](https://doi.org/10.1016/j.jag.2020.102050).
- [46] Z.-W. Li, X.-L. Ding, D.-W. Zheng, and C. Huang, "Least squares-based filter for remote sensing image noise reduction," *IEEE Trans. Geosci. Remote Sens.*, vol. 46, no. 7, pp. 2044–2049, Jul. 2008, doi: [10.1109/TGRS.2008.916981](https://doi.org/10.1109/TGRS.2008.916981).
- [47] X. Xing, L. Huang, Z. He, T. Zhang, and Y. Zhu, "Health observation of the capital airport south expressway based on improved MT-InSAR technology," *IEEE J. Miniaturization Air Space Syst.*, vol. 4, no. 3, pp. 232–241, Nov. 2023, doi: [10.1109/JMASS.2023.3260098](https://doi.org/10.1109/JMASS.2023.3260098).
- [48] C. Yu, N. T. Penna, and Z. Li, "Generation of real-time mode high-resolution water vapor fields from GPS observations," *J. Geophys. Res. Atmos.*, vol. 122, no. 3, pp. 2008–2025, Feb. 2017, doi: [10.1002/2016JD025753](https://doi.org/10.1002/2016JD025753).
- [49] C. Yu, Z. Li, and N. T. Penna, "Interferometric synthetic aperture radar atmospheric correction using a GPS-based iterative tropospheric decomposition model," *Remote Sens. Environ.*, vol. 204, pp. 109–121, Jan. 2018, doi: [10.1016/j.rse.2017.10.038](https://doi.org/10.1016/j.rse.2017.10.038).
- [50] L. Zhang, X. He, T. Balz, X. Wei, and M. Liao, "Rational function modeling for spaceborne SAR datasets," *ISPRS J. Photogramm. Remote Sens.*, vol. 66, no. 1, pp. 133–145, Jan. 2011, doi: [10.1016/j.isprsjprs.2010.10.007](https://doi.org/10.1016/j.isprsjprs.2010.10.007).
- [51] C. Rossi, M. Eineder, T. Fritz, and H. Breit, "TanDEM-X mission: Raw DEM generation," in *Proc. 8th Eur. Conf. Synth. Aperture Radar*, Jun. 2010, pp. 1–4.

- [52] W. Tang, M. Wang, P. Li, G. Wang, Y. Yan, and W. Yan, "Ground subsidence associated with mining activity in the ningdong coal base area, northwestern China revealed by InSAR time series analysis," *Frontiers Earth Sci.*, vol. 11, Jul. 2023, Art. no. 1132890, doi: [10.3389/feart.2023.1132890](https://doi.org/10.3389/feart.2023.1132890).
- [53] P. Li, H. Qian, and J. Wu, "Environment: Accelerate research on land creation," *Nature*, vol. 510, no. 7503, pp. 29–31, Jun. 2014, doi: [10.1038/510029a](https://doi.org/10.1038/510029a).
- [54] X. Hu et al., "Remote sensing characterization of mountain excavation and city construction in loess Plateau," *Geophys. Res. Lett.*, vol. 48, no. 21, pp. 1–11, Oct. 2021, doi: [10.1029/2021gl095230](https://doi.org/10.1029/2021gl095230).



Tengfei Zhang (Graduate Student Member, IEEE) received the B.S. degree in geomatics and surveying from Zhengzhou Technology and Business University, Zhengzhou, China, in 2020, and the M.S. degree in surveying and mapping science and technology from Changsha University of Science and Technology, Changsha, China, in 2023. He is currently pursuing the Ph.D. degree with the School of Resource and Environment Science, Wuhan University, Wuhan, China.

His research interests include the application of InSAR technology for high-precision DEM reconstruction and deformation monitoring in salt solution mining.



Yumin Chen is currently a Professor and a Doctoral Supervisor with the School of Resource and Environmental Sciences, Wuhan University, Wuhan, China. Her research interests include the dynamic simulation of surface processes, spatial information artificial intelligence, remote sensing applications to environment issues, and big data intelligent processing and analysis.



Lu Zhang received the B.Eng. and M.Eng. degrees in computer science and technology from Wuhan University of Hydraulic and Electrical Engineering, Wuhan, China, in 1997 and 2000, respectively, and the Ph.D. degree in photogrammetry and remote sensing from Wuhan University, Wuhan, in 2005. From 2005 to 2007, he was a Post-Doctoral Research Fellow with the Institute of Space and Earth Information Science, Chinese University of Hong Kong, Hong Kong. Since 2007, he has been with the State Key Laboratory of Surveying, Mapping and Remote Sensing, Wuhan University, where he became a Full Professor in 2013. He was involved in several research projects funded by the National Natural Science Foundation of China and the Ministry of Science and Technology. In recent years, he has authored or co-authored more than 40 peer-reviewed scientific articles. His research interests include synthetic aperture radar interferometry as well as remote sensing classification and change detection.



John P. Wilson received the Ph.D. degree from the University of Toronto, Toronto, ON, Canada, in 1986.

He is a Professor of spatial sciences and sociology at the Dana and David Dornsife College of Letters, Arts and Sciences, University of Southern California (USC), Los Angeles, CA, USA, where he is the Founding Director of the Spatial Sciences Institute. He was the Chair of the Department of Geography, USC. He has published numerous books and articles on these topics, including two edited volumes,

Terrain Analysis: Principles and Applications (John Wiley and Sons, 2000) and *The Handbook of Geographic Information Science* (Blackwell Publishers, 2007), and *Environmental Applications of Digital Terrain Modeling* (John Wiley and Sons, 2018). His research interests include the modeling of environmental systems and makes extensive use of GIS software tools, fieldwork, spatial analysis techniques, and computer models.

Dr. Wilson currently serves as the Editor-in-Chief for the UCGIS GIST Body of Knowledge Project and is an active participant in the UNIGIS International Network and a worldwide consortium of universities focused on online geographic information science academic programs.



Rui Zhu received the Ph.D. degree from The Hong Kong Polytechnic University, Hong Kong, China, in 2018.

He is a Senior Scientist at the Institute of High Performance Computing, Agency for Science, Technology and Research, Singapore. He was a Research Assistant Professor at The Hong Kong Polytechnic University and a Post-Doctoral Associate at MIT Senseable City Laboratory, Cambridge, MA, USA. His study focused on GIScience, urban informatics, and solar energy with a publication of

more than 70 SCI articles in journals, such as *Nature Communications*, *The Innovation*, and *Science Bulletin*.

Dr. Zhu is an Associate Editor of *Computer Science* (Springer Nature), an Editor of *Big Earth Data* and *Advances in Applied Energy*, and a Young Editor of *The Innovation*. He is also the PI/Co-I for several research grants and the Board of Director Member of Chinese Professional in Geographic Information Systems. His study has been reported by international media, such as Singapore TV, Lianhe Zaobao, and MIT News.



Ruoxuan Chen received the B.S. degree in geographic information science from Yunnan University, Kunming, China, in 2023. She is currently pursuing the M.S. degree with the School of Resource and Environment Science, Wuhan University, Wuhan, China.

Her research interests include the super-resolution reconstruction of DEM.



Zhanghui Li received the B.S. degree in geographic information science from Wuhan University, Wuhan, China, in 2023, where he is currently pursuing the M.S. degree with the School of Resource and Environmental Sciences.

His research interests include image fusion and cloud removal in satellite data.